Research article

JHEP|Reports

Glycogen synthase kinase 3 activity enhances liver inflammation in MASH

Mireille Khoury,[1,†] **Qianqian Guo**,[1,†] Kunimaro Furuta,[1,2] Cristina Correia,[3] Chady Meroueh,[4] Hyun Se Kim Lee,[1] Khaled Warasnhe,[1] Lucía Valenzuela-Pérez,[1] Andrew P. Mazar,[5] Iljung Kim,[6] Yung-Kyun Noh,[6,7] Heather Holmes,[8] Michael F. Romero,[8,9] Caroline R. Sussman,[9] Kevin D. Pavelko,[10] Shahidul Islam,[1] Adebowale O. Bamidele,[1,11] Petra Hirsova,[1] Hu Li,[3] Samar H. Ibrahim[1,12,*]

[1]*Division of Gastroenterology & Hepatology, Mayo Clinic, Rochester, MN, USA;* [2]*Department of Gastroenterology and Hepatology, Osaka University Graduate School of Medicine, Osaka, Japan;* [3]*Center for Individualized Medicine, Department of Molecular Pharmacology and Experimental Therapeutics, Mayo Clinic College of Medicine and Science, Rochester, MN, USA;* [4]*Division of Anatomic Pathology, Mayo Clinic, Rochester, MN, USA;* [5]*Actuate Therapeutics Inc, Fort Worth, TX, USA;* [6]*Department of Computer Science, Hanyang University, Seoul, Republic of Korea;* [7]*School of Computational Sciences, Korea Institute for Advanced Study, Seoul, Republic of Korea;* [8]*Department of Physiology and Biomedical Engineering, Mayo Clinic, Rochester, MN, USA;* [9]*Division of Nephrology and Hypertension, Mayo Clinic, Rochester, MN, USA;* [10]*Immune Monitoring Core, Mayo Clinic, Rochester, MN, USA;* [11]*Department of Immunology, Mayo Clinic, Rochester, MN, USA;* [12]*Division of Pediatric Gastroenterology & Hepatology, Mayo Clinic, Rochester, MN, USA*

JHEP Reports **2024.** https://doi.org/10.1016/j.jhepr.2024.101073

Background & Aims: Metabolic dysfunction-associated steatohepatitis (MASH) is characterized by excessive circulating toxic lipids, hepatic steatosis, and liver inflammation. Monocyte adhesion to liver sinusoidal endothelial cells (LSECs) and transendothelial migration (TEM) are crucial in the inflammatory process. Under lipotoxic stress, LSECs develop a proinflammatory phenotype known as endotheliopathy. However, mediators of endotheliopathy remain unclear.

Methods: Primary mouse LSECs isolated from C57BL/6J mice fed chow or MASH-inducing diets rich in fat, fructose, and cholesterol (FFC) were subjected to multi-omics profiling. Mice with established MASH resulting from a choline-deficient high-fat diet (CDHFD) or FFC diet were also treated with two structurally distinct GSK3 inhibitors (LY2090314 and elraglusib [9-ING-41]).

Results: Integrated pathway analysis of the mouse LSEC proteome and transcriptome indicated that leukocyte TEM and focal adhesion were the major pathways altered in MASH. Kinome profiling of the LSEC phosphoproteome identified glycogen synthase kinase (GSK)-3β as the major kinase hub in MASH. GSK3β-activating phosphorylation was increased in primary human LSECs treated with the toxic lipid palmitate and in human MASH. Palmitate upregulated the expression of C-X-C motif chemokine ligand 2, intracellular adhesion molecule 1, and phosphorylated focal adhesion kinase, via a GSK3-dependent mechanism. Congruently, the adhesive and transendothelial migratory capacities of primary human neutrophils and THP-1 monocytes through the LSEC monolayer under lipotoxic stress were reduced by GSK3 inhibition. Treatment with the GSK3 inhibitors LY2090314 and elraglusib ameliorated liver inflammation, injury, and fibrosis in FFC- and CDHFD-fed mice, respectively. Immunophenotyping using cytometry by mass cytometry by time of flight of intrahepatic leukocytes from CDHFD-fed mice treated with elraglusib showed reduced infiltration of proinflammatory monocyte-derived macrophages and monocyte-derived dendritic cells.

Conclusion: GSK3 inhibition attenuates lipotoxicity-induced LSEC endotheliopathy and could serve as a potential therapeutic strategy for treating human MASH.

Impact and Implications: LSECs under lipotoxic stress in MASH develop a proinflammatory phenotype known as endotheliopathy, with obscure mediators and functional outcomes. The current study identified GSK3 as the major driver of LSEC endotheliopathy, examined its pathogenic role in myeloid cell-associated liver inflammation, and defined the therapeutic efficacy of pharmacological GSK3 inhibitors in murine MASH. This study provides preclinical data for the future investigation of GSK3 pharmacological inhibitors in human MASH. The results of this study are important to hepatologists, vascular

Keywords: Glycogen synthase kinase 3 (GSK3); Non-alcoholic steatohepatitis (NASH); Metabolic dysfunction associated steatohepatitis (MASH); Liver sinusoidal endothelial cells (LSEC); Myeloid cells; Inflammation; Chemokines; Adhesion; Migration; Liver fibrosis.

Received 6 June 2023; received in revised form 12 March 2024; accepted 20 March 2024; available online 26 March 2024

† These authors contributed equally to this work.

* Corresponding author. Address: Division of Pediatric Gastroenterology, Department of Pediatric and Adolescent Medicine, Mayo Clinic, 200 First Street SW, Rochester, MN 55905, USA. Tel.: +1 507 266 0114; Fax: +1 507 284 0160.

E-mail address: ibrahim.samar@mayo.edu (S.H. Ibrahim).

biologists, and investigators studying the mechanisms of inflammatory liver disease and MASH, as well as those interested in drug development.

Introduction

Metabolic dysfunction-associated steatohepatitis (MASH) is a growing public health problem,[1] and its pathogenesis involves both lipotoxicity (toxic lipid-induced cellular stress)[2] and a sterile inflammatory response.[3] Similar to other liver cell types affected in MASH, lipotoxicity in liver sinusoidal endothelial cells (LSECs) triggers aberrant signaling, resulting in structural and functional alterations leading to LSEC dysfunction and a proinflammatory phenotype, which we refer to here as endotheliopathy.[4–6] Emerging data implicate LSEC endotheliopathy in liver inflammation in MASH.[7,8] Increased LSEC capillarization has been reported in mice with diet-induced MASH, as evidenced by reduced fenestrae and Lyve 1 expression (a marker of well-differentiated LSECs), and increased CD34 expression (a marker of capillarized LSECs).[9] In the current study, we examine the molecular mediators and functional outcome of lipotoxic LSEC endotheliopathy as it relates to MASH pathogenesis.

The inflammatory response in MASH is mainly mediated by recruited proinflammatory myeloid cells and their homing to the MASH liver.[10,11] Two of the crucial mechanisms involved in this process are the chemotaxis and adhesion of myeloid cells to LSECs.[12] Although a growing body of evidence implicates LSEC dysfunction in various liver diseases, including MASH,[13] few studies have focused on targeting molecular mediators of myeloid cell adhesion to LSECs in MASH.[7,14] Circulating myeloid cells exit the vasculature to achieve residence in the MASH liver, a process known as transendothelial migration (TEM). TEM is often preceded by leukocyte adhesion, a crucial step in the inflammatory response. It occurs via the paracellular route (at the adherence junction) or transcellular route (through transcellular channels). Paracellular TEM, the most common route of TEM for myeloid cells, is mediated by the disassembly of the adherence junctions.[15] Most leukocytes that adhere to the endothelial wall at the site of inflammation re-enter the circulation. However, once leukocytes commit to TEM, they migrate through the hepatic parenchyma to fuel the inflammatory process.[16]

Glycogen synthase kinase (GSK)-3 is a primary serine/threonine kinase that integrates multiple signaling pathways, including cell metabolism, adhesion, and inflammation.[17] It has two ubiquitously expressed and highly conserved isoforms (α and β), with both shared and distinct substrates and functional effects. Aberrant GSK3 activation is pathogenic in numerous inflammatory diseases, and GSK3 inhibitors in rodent models have been successful in curtailing exuberant inflammatory responses.[18,19] Furthermore, GSK3β has been implicated in pulmonary vascular endothelial barrier dysfunction.[20] In addition, GSK3α promotes fatty acid uptake and lipotoxic cardiomyopathy in murine models of diet-induced obesity.[21] However, the biological consequences of lipotoxicity-induced aberrant GSK3 activation in LSEC, as well as the potential therapeutic ramifications of inhibiting GSK3 enzymatic activity during MASH, are largely unknown.

Herein, using phosphoproteomics and kinome profiling in mouse LSECs, we report that GSK3β serves as a major hub and the main kinase in MASH, thereby acting as a potential driver of lipotoxic endotheliopathy. Furthermore, we show that GSK3β in LSECs mediates key elements of TEM: (i) expression of chemokines, namely C-X-C motif chemokine ligand (CXCL)-2; and (ii) density of adhesion molecules, namely intracellular adhesion molecule 1 (ICAM-1). Most importantly, using established diet-induced mouse models of MASH, we identified that pharmacological inhibition of GSK3 using two structurally distinct inhibitors that have been used in human clinical trials (NCT01287520 and NCT04218071) ameliorates liver injury, inflammation, and fibrosis, mainly by reducing myeloid cell infiltration into the liver.

Materials and methods

The full details of the materials and methods are provided in the supplementary data online.

Results

GSK3β is the top hub kinase altered in MASH LSECs

To obtain a comprehensive and in-depth understanding of the LSEC phenotype and intracellular signaling networks during MASH, we performed phospho- and total proteomic analyses on LSECs isolated from mice fed either a chow or a fat, fructose, and cholesterol (FFC) diet for 24 weeks. The FFC diet is a well-established MASH mouse model that phenocopies the metabolic and histological features of the human disease (Fig. 1A).[7,22] We performed an integrated pathway analysis of the total proteomic data and our previously generated LSEC transcriptomic data (GSE164006).[7] We selected genes (or protein-coding genes) that were differentially regulated between chow-fed and FFC-fed mice using LSEC total proteomic or RNA-sequencing (RNA-seq). We reasoned that focusing on genes showing consistent directionality changes in both layers of 'omics' might provide insights into the underlying biological aspects of the disease. Hence, we subjected all mRNA-protein correlated genes (orange and blue dots in Fig. 1B) to a Kyoto Encyclopedia of Genes and Genomes (KEGG) over-representation pathway analysis (Fig. 1C). We identified leukocyte TEM (p = 5.96E-04) and focal adhesion (p = 2.94E-04) among the top-10 canonical pathways altered in MASH LSECs. These findings are consistent with emerging literature implicating monocyte adhesion to endothelial cells and TEM in the sterile inflammatory process in MASH.[23] Next, we performed kinome enrichment analysis[24] of the LSEC phosphoproteomic data based on the phosphorylation status of putative substrates of kinases. Notably, GSK3β was identified as the major hub (Fig. 1D) on the kinome map and the top-ranked kinase with altered activity in MASH (p = 1.58E-03) (Fig. 1E and Fig. S1). To further confirm the findings obtained from murine phosphoproteomics and explore their relevance to human biology, we examined whether GSK3 is activated in human LSECs under lipotoxic stress. To this end, we used the saturated free fatty acid (FFA) palmitate (PA) to induce lipotoxicity *in vitro*. PA contributes to the majority of circulating saturated FFA in human MASH,[25] and its lipotoxic impact on LSECs has been previously established.[7] First, we showed in primary human LSECs that phosphorylation of tyrosine residues (Y279 for GSK3α and Y216 for

GSK3β), which are known to enhance the enzymatic activity of both GSK3[26] and glycogen synthase (GS), a specific GSK3 substrate, increased with PA treatment. Furthermore, GS phosphorylation in primary human LSECs was reduced by treatment with the GSK3 pharmacological inhibitor LY2090314 (LY) (Fig. 1F). Likewise, in a mouse LSEC cell line, known as transformed mouse LSECs (TSECs), phosphorylation of GSK3α/β (Y279/216) and GS was increased by PA treatment (Fig. 1G). We also confirmed the sequential phosphorylation of GSK3 and GS using TSECs treated with the FFA toxic intracellular metabolite lysophosphatidylcholine (LPC) (Fig. 1H).[27] Collectively, these findings confirm that GSK3 is activated in human and mouse LSECs under lipotoxic stress and in mice with diet-induced MASH.

GSK3 mediates toxic lipid-induced proinflammatory responses in LSECs

Next, we investigated whether toxic lipid-induced GSK3 activation promotes LSEC proinflammatory phenotypes. To obtain a comprehensive human LSEC transcript data set, we treated primary human LSECs with (i) vehicle (Veh), (ii) PA, or (iii) PA with LY, and subjected the isolated RNA to a NanoString-based mRNA profiling assay, which can quantify the copy numbers of 760 fibrosis-related human genes.[28] In total, 479 genes were

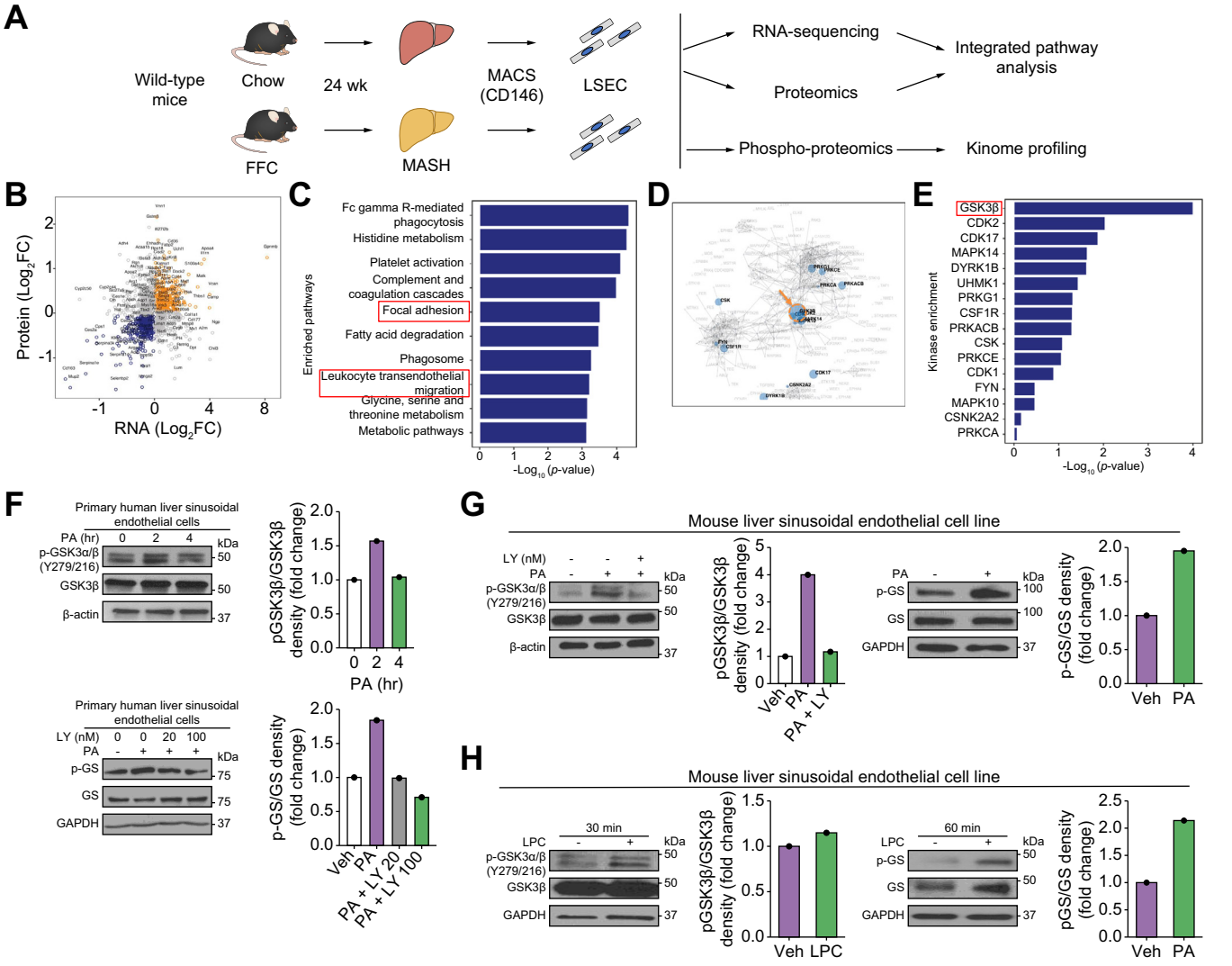

Fig. 1. Glycogen synthase kinase (GSK)-3β is a central mediator of liver sinusoidal endothelial cell (LSEC) endotheliopathy in metabolic dysfunction-associated steatohepatitis (MASH). (A) Schematic of the *in vivo* multi-omics study. (B) Scatter plot showing differentially expressed genes (p <0.05) in chow *vs.* fat, fructose, and cholesterol (FFC)-fed mice based on either LSEC total proteomic or RNA-sequencing (RNA-seq) analysis. The x- and y-axes represent the log 2-converted fold change (log_2FC) of the signals in FFC- *vs.* chow-fed mice in the proteomic and RNA-seq studies, respectively. (C) Top-10 enriched pathways representative of the differentially regulated genes in FFC *vs.* chow-fed mice based on both proteomics and RNA-seq analyses. (D) Kinome map generated from the phosphoproteomic study shown in A. (E) Top-16 ranked putative altered kinases in FFC *vs.* chow-fed mice. (F) Primary human LSECs were treated with the vehicle (Veh), 500 μM palmitate (PA), or 500 μM PA ± the GSK3 inhibitor LY2090314 (LY). Protein levels of phosphorylated (p)-GSK3α/β (Y279/216) and GSK3β (top) and phosphorylated glycogen synthase (p-GS) and glycogen synthase (GS) (bottom) were assessed using Western blotting. (G) A mouse LSEC line was treated with Veh or 500 μM PA ± 20 nM LY for 4 h, and the protein levels of p-GSK3α/β (Y279/216) and GSK3β were assessed (left). Mouse LSEC lines were also treated with Veh or 500 μM PA for 2 h and p-GS and GS were assessed. (H) A mouse LSCE line was treated with Veh or lysophosphatidylcholine (LPC), and the protein levels of p-GSK3α/β (Y279/216), GSK3β, p-GS, and GS were assessed. β-Actin or glyceraldehyde-3-phosphate dehydrogenase (GAPDH) was used as loading control. F–H were repeated for at least three times; representative results are shown with quantification.

detected, 31 of which were abundant in cells treated with PA *vs.* Veh and categorized as 'lipotoxic stress-dependent genes', and 154 genes were upregulated in cells treated with PA *vs.* PA with LY and categorized as 'GSK3-dependent genes' (Fig. 2A). To further narrow down the gene candidates that are likely essential in MASH pathogenesis across human and mouse species, we used our LSEC RNA-seq data from FFC diet-induced MASH. Genes upregulated in MASH *vs.* chow mice were categorized as 'MASH-dependent genes'. Ten genes overlapped among the three categories defined above. Among these, we focused on *ICAM1* and *CXCL2*, which encode the adhesion molecule ICAM-1 and CXCL2, respectively. Our selection was based on the potential of ICAM-1 and CXCL2 acting in concert during myeloid cell transmigration across the sinusoidal endothelium. These findings were confirmed by conventional quantitative (q)PCR, showing the upregulation of *ICAM1* and *CXCL2* in PA-treated LSECs and the reduction in expression of these genes by inhibition of GSK3 function with LY treatment or GSK3β small interfering (si)RNA transfection (Fig. 2B and D). Interestingly, the increased expression of *ICAM1* and *CXCL2* induced by the proinflammatory cytokine tumor necrosis factor (TNF)-α was not reduced by GSK3 inhibition (Fig. 2C), suggesting that GSK3 selectively promotes the proinflammatory phenotype in LSECs downstream of the lipotoxic signal.

To assess the zonal distribution of lipotoxic endotheliopathy across the hepatic lobule *in vivo*, we used ICAM-1 as a marker of MASH endotheliopathy and scanned whole *ICAM1*-immunostained slides from mice with FFC diet-induced MASH and chow

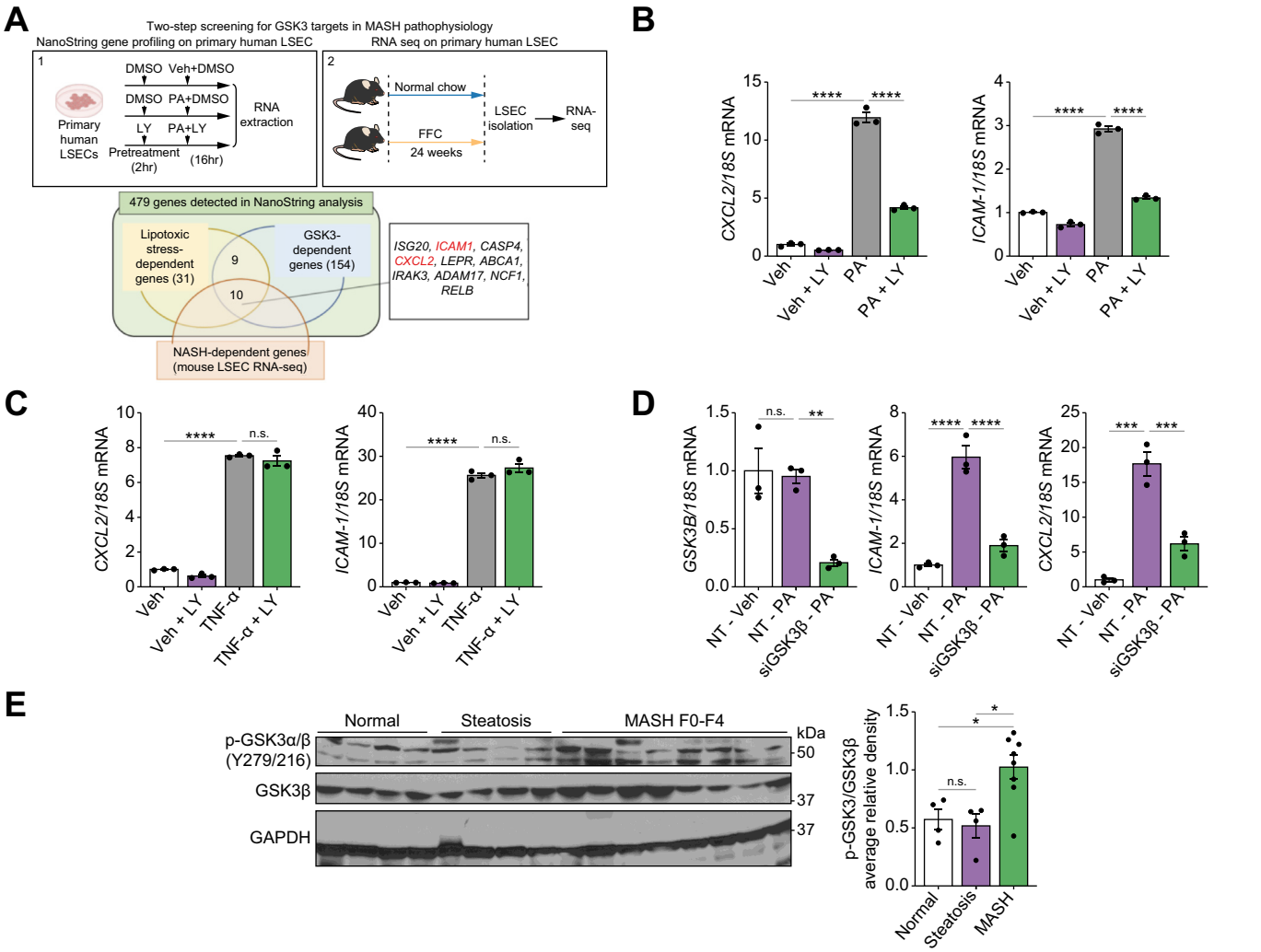

Fig. 2. Glycogen synthase kinase (GSK)-3 mediates toxic lipid-induced proinflammatory responses in liver sinusoidal endothelial cells (LSECs). (A) Primary human LSECs were treated with vehicle (Veh) or 500 μM palmitate (PA) ± 20 nM LY2090314 (LY) for 16 h, and gene expression profiling was performed using the NanoString nCounter system (1). LSECs were isolated from chow- and fat, fructose, and cholesterol (FFC)-fed mice and subjected to RNA-sequencing (RNA-seq) (2). Venn diagram (bottom) of genes classified as 'lipotoxic stress-dependent genes' and 'GSK3-dependent genes' in NanoString analysis and 'Metabolic dysfunction-associated steatohepatitis (MASH)-dependent genes' in mouse LSEC RNA-seq. Primary human LSECs were treated with Veh or 500 μM of PA (B) or 10 ng/ml tumor necrosis factor (TNF)-α (C) ± 20 nM LY for 16 h, and mRNA expression of C-X-C motif chemokine ligand 2 (*CXCL2*) and intracellular adhesion molecule 1 (*ICAM1*) was examined. (D) Primary human LSECs were transfected with siGSK3β or non-target small interfering (si)RNA for 72 h, then treated with Veh or 500 μM PA for 24 h, and the mRNA expression of *GSK3B*, *CXCL2*, and *ICAM1* was examined (n = 3 per group). (E) Phospho-GSK3α/β (Y279/216) and GSK3β protein levels were assessed in normal controls and patients with steatosis, and MASH by Western blotting with quantification. Glyceraldehyde-3-phosphate dehydrogenase (GAPDH) was used as the loading control (n = 4–8 per group). Bar graphs represent mean ± SEM; $^{*}p$ <0.05, $^{**}p$ <0.01, $^{***}p$ <0.001, $^{****}p$ <0.0001, ns, non-significant (one-way ANOVA with Bonferroni's multiple comparison).

controls. The liver pathologist manually annotated the zones of the liver lobules and used a machine learning algorithm to analyze the zonal changes in *ICAM1* expression (Fig. S2A and B), showing no zonal difference in the expression of *ICAM1* or the percentage of steatotic area (Fig. S2C). These findings suggest that LSEC endotheliopathy in MASH is present across all liver zones. To confirm that the role of GSK3 in MASH pathogenesis is conserved in human disease, we performed Western blotting on human liver samples and confirmed increased GSK3α/β (Y279/216) phosphorylation in patients with MASH compared with patients with steatosis and normal subjects (Fig. 2E). Collectively, these observations support the concept that GSK3 activation promotes a proinflammatory phenotype in LSECs under lipotoxic stress, culminating in endotheliopathy.

GSK3 activation in LSECs under lipotoxic stress enhances myeloid cell adhesion and TEM

TEM of myeloid cells is a key biological process in their recruitment to sites of inflammation, and is associated with reduced endothelial barrier integrity.[15] Activated focal adhesion kinase (FAK) in endothelial cells promotes the phosphorylation of vascular endothelial cadherin (VE-cadherin). Phosphorylated VE-cadherin dissociates from β-catenin, leading to the displacement of β-catenin from cell adherens junctions, widening of cell–cell junctions, and disruption of endothelial barrier integrity (Fig. 3A).[29] Given that FAK is a known substrate of GSK3, we sought to determine the effect of activated GSK3 on FAK phosphorylation in LSECs under lipotoxic stress. We found that PA treatment enhanced FAK phosphorylation in LSECs, which was attenuated by GSK3 inhibition with LY (Fig. 3B). Enhanced phosphorylation of FAK during lipotoxic stress in a GSK3-dependent manner was also associated with increased VE-cadherin phosphorylation (Fig. 3B) and intracellular expression (Fig. 3C). Moreover, we observed reduced β-catenin intensity around the cell–cell junction in response to PA (Fig. 3D), which is suggestive of adherens junction disassembly essential for TEM and hepatic infiltration of recruited myeloid cells during MASH.

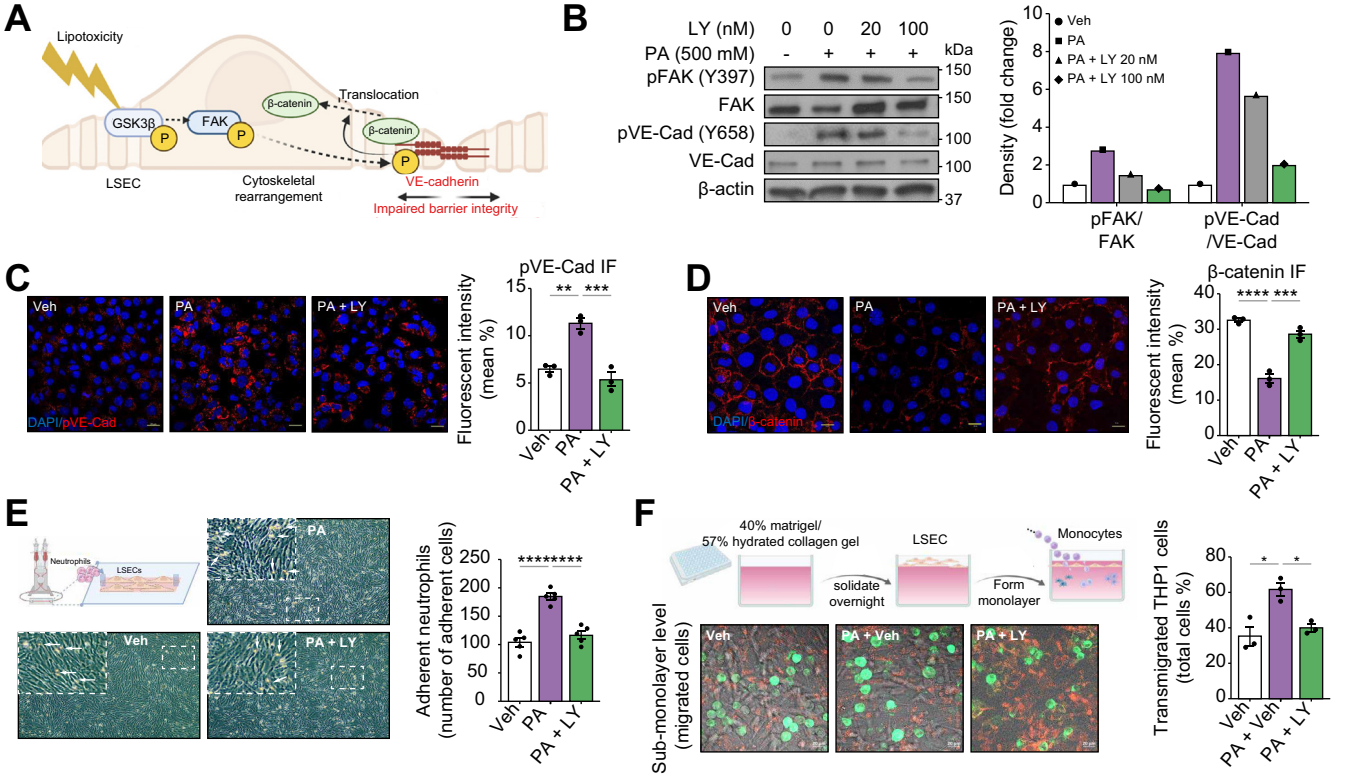

Fig. 3. Glycogen synthase kinase (GSK)-3 mediates liver sinusoidal endothelial cell (LSEC) lipotoxicity-induced monocyte transendothelial migration (TEM). (A) Schematic showing that lipotoxicity-induced GSK3β activation triggers a multistep phosphorelay signal transduction mechanism (GSK3β–focal adhesion kinase [FAK]–vascular endothelial [VE]-cadherin), leading to LSEC cytoskeletal rearrangement, adherence junction disassembly, and β-catenin dissociation from VE-cadherin and internalization, resulting in endothelial barrier dysfunction. (B) Primary human LSECs were treated with vehicle (Veh) or 500 μM palmitate (PA) ± LY2090314 (LY) at the indicated concentrations for 4 h, and protein levels of phosphorylated FAK (p-FAK), total FAK, phosphorylated (p)-VE-cadherin, and total VE-cadherin were assessed by Western blotting. β-Actin was used as a loading control. B was repeated at least three times, and representative results are shown, along with quantification. (C) Localization of p-VE-cadherin was assessed using immunofluorescence and quantified (right). (D) β-Catenin localization was assessed by immunofluorescence and quantified (right). DAPI was used for the nuclear staining. (E) Schematic of the flow-based neutrophil adhesion assay. Representative microscopic images of neutrophils adherent to primary human LSECs under the three experimental conditions. White arrows indicate adherent neutrophils. Five random fields in a 20 × microscopic field for each condition were captured and quantified (right). (F) Schematic of the collagen gel-based TEM assay. Representative images from confocal microscopy for the TEM assay at 1 h (left). THP-1 cells (green fluorescence) in focus on the apical surface of the endothelial monolayer (red fluorescence) were defined as non-migrated, those in focus below the plane of the endothelial monolayer were defined as transmigrated, and three random fields in a 63 × microscopic field from each condition were captured and quantified. Bar graphs represent mean ± SEM; **p* <0.05, ***p* <0.01, ****p* <0.001, *****p* <0.0001 (one-way ANOVA with Bonferroni's multiple comparison; n = 3–5 per group). Scale bars: 20 μm (C,D,F).

Next, we examined whether toxic lipid-induced activation of GSK3 in LSECs enhanced myeloid cell adhesion and TEM. A flow-based adhesion assay (Fig. 3E) showed reduced adhesion of primary human neutrophils to LSECs pretreated with PA and LY. Next, we assessed the impact of GSK3 inhibition on the TEM of myeloid cells through an LSEC monolayer under lipotoxic stress. The TEM assay using a Transwell system with a porous membrane-assembled insert has intrinsic limitations in that the fluid media at the bottom chamber does not reproduce well the colloidal extracellular matrix of the space of Disse, and LSECs plated on the membrane can migrate through the pore, which complicates the analysis of the data. Hence, we utilized a previously used system with minor modifications to mimic the liver sinusoidal milieu; Vybrant DiI-labeled LSECs were plated directly onto a hydrated collagen gel to form a monolayer, and the migration of the DiO-labeled monocytic cell line THP-1 was assessed using confocal microscopy.[30] Our data indicated an increase in the number of THP-1 cells that migrated through the Veh-pretreated LSEC monolayer into the collagen gel in response to PA treatment, in contrast to LSEC pretreated with LY20930314, where there was a significant reduction in migrated THP-1 cells, suggesting that myeloid cell TEM in response to lipid-induced signals in LSECs is mediated by intrinsic GSK3 enzymatic activity (Fig. 3F). Taken together, these data support a crucial role for LSEC GSK3 during lipotoxicity in myeloid cell TEM.

GSK3 inhibition with LY2090314 ameliorates FFC diet-induced murine MASH

Based on our *in vitro* findings supporting the proinflammatory role of aberrant GSK3 activation in LSECs under lipotoxic stress, we examined the potential beneficial effect of GSK3 inhibition in mice with FFC diet-induced MASH. Chow- or FFC-fed mice were treated with Veh or the GSK3 inhibitor LY three times a week for 4 weeks (Fig. 4A). We elected to use LY given its established safety and tolerability in humans.[31] First, we examined the metabolic phenotypes of these mice. Daily caloric intake, body weight, and homeostasis model assessment of insulin resistance (HOMA-IR) (Fig. S3A) were increased with the FFC diet but were similar in the Veh-treated *vs.* LY-treated groups. Furthermore, LY treatment was well tolerated, and the physical activity, respiratory quotient, metabolic rate, and percentage of lean and fat masses when assessed by the comprehensive laboratory animal monitoring system and echo-magnetic resonance imaging were also similar between the Veh and LY treatment groups on the FFC diet (Fig. S3B and C). Furthermore, the liver-to-body weight ratio (Fig. 4B) and hepatic triglyceride content (Fig. 4C) in the FFC mice were reduced by LY treatment. However, steatosis was not significantly reduced by LY treatment in MASH mice (Fig. 4D). This observation was confirmed by automated quantification of steatosis percentage on the whole digitized H&E-stained slides (Fig. S4A and B), as well as by steatosis scoring (Fig. S4C) by estimating the steatotic area percentage in five fields per mouse and then taking the average (score 1 [6–33%], score 2 [33–66%], score 3 [>66%]). Similarly, hepatocyte ballooning was not altered by LY treatment (Fig. S4D). Taken together, these data suggest a minor role for GSK3 inhibition in steatosis and other metabolic alterations in murine MASH.

Given the key role of LSEC GSK3 in myeloid cell adhesion and TEM (Fig. 3E and F), we examined whether GSK3 inhibition reduces macrophage and neutrophil hepatic infiltration. Immunostaining of liver tissues indicated that LY-treated mice had a reduced positive area for the macrophage marker F4/80 (Fig. 4E) and the neutrophil marker myeloperoxidase (MPO) (Fig. S5A). Interestingly, the expression of the LSEC endotheliopathy marker ICAM-1 (Fig. 4F) was increased with FFC feeding and reduced with LY treatment, whereas the marker of differentiated LSEC Lyve-1 was reduced in FFC mice and restored with LY treatment (Fig. S5B). Similarly, *Cxcl2* mRNA expression increased with the FFC diet and decreased with LY treatment (Fig. 4G). These data support the role of GSK3 in the proinflammatory phenotypes of LSECs in MASH and are consistent with our *in vitro* findings.

Moreover, FFC-induced liver injury was attenuated by GSK3 inhibition as assessed by reduced plasma alanine aminotransferase (ALT) levels (Fig. 4H) and apoptotic hepatocytes by terminal deoxynucleotidyl transferase dUTP nick-end labeling (TUNEL)-positive cells (Fig. 4I) in LY-treated mice.

Finally, to determine whether GSK3 inhibition can mitigate liver fibrosis, the most important factor associated with morbidity and mortality in MASH,[32] we performed ultrasound-based liver elastography 4 weeks after the initiation of treatment with LY. Liver stiffness was assessed by the Young's modulus (YM), which was increased in FFC-fed mice but reduced with LY treatment (Fig. 5A). Likewise, FFC-fed LY-treated mice showed a reduced Sirius Red-positive area compared with Veh-treated mice on the same diet when quantified by morphometry (Fig. 5B), indicating a therapeutic effect of LY against MASH-associated liver fibrosis. Similarly, fiber density (when assessed by CT-FIRE, an academic software package available as a free download developed by the Eliceiri lab at UW Madison) was reduced in FFC-fed mice treated with LY (p <0.01; Fig. 5C). Overall, collagen fiber density was positively correlated with YM (Pearson's correlation coefficient, r = 0.70) (Fig. 5D). Collagen fibers were narrower and longer with the FFC diet than with the chow controls, with no change in straightness in the FFC treatment group *vs.* no treatment group (Fig. S6). These findings were further confirmed by immunostaining of the liver for alpha-smooth muscle actin (α-SMA), a hepatic stellate cell activation marker (Fig. 5E), and mRNA expression of the genes encoding α-SMA (*Acta2*) and Collagen 1a1 (*Col1a1*) (Fig. 5F). Taken together, these findings suggest that pharmacological inhibition of GSK3 ameliorates liver inflammation, injury, and fibrosis in diet-induced MASH.

GSK3 inhibition with elraglusib (9-ING-41) ameliorates CDHFD-induced murine MASH

To further confirm the role of GSK3β in the recruitment of proinflammatory myeloid cells to the liver, we used 9-ING-41, a more selective GSK3β inhibitor that is structurally distinct from LY [at 10 μM, 9-ING-41 was found to inhibit GSK3β by 97% and GSK3α by 92% (GSK3β IC_{50} = 635 nM)]. To validate our findings in a different MASH mouse model, we used a choline-deficient high-fat diet (CDHFD; A06071302, Research Diet), a well-established MASH mouse model that induces pronounced myeloid cell-associated liver inflammation and fibrosis in 6 weeks.[7,33] Mice were treated with either Veh or 9-ING-41 at a dose of 30 mg/kg per day intraperitoneally for 2 weeks during the final 2 weeks of the feeding study (Fig. 6A). The liver-to-body weight ratio was not altered by 9-ING-41 treatment in CDHFD-fed mice (Fig. S7A). Steatosis, lobular inflammation, and hepatocyte ballooning were assessed using the NASH Clinical Research Network Scoring System (NAS), which was reduced in CDHFD-fed 9-ING-41-treated mice (Fig. 6B and Fig. S7B), mainly secondary to reduced inflammation. Immunofluorescence and confocal microscopy showed increased neutrophil infiltration in

CDHFD-fed mice when assessed by MPO staining, which was reduced with 9-ING-41 treatment (Fig. 6C). Likewise, immunostaining of liver tissues revealed that 9-ING-41-treated mice had a reduced positive area for macrophage marker F4/80 (Fig. 6D). Moreover, the mRNA expression of the proinflammatory monocyte marker Ccr2 increased with the CDHFD diet and decreased with 9-ING-41 treatment (Fig. 6E), suggesting that inhibition of GSK3 reduces myeloid cell infiltration in the MASH liver parenchyma. Furthermore, 9-ING-41 treatment reduced liver injury, as assessed by ALT levels (Fig. 6F). Monocyte adhesion to LSECs increased in the LSECs of Veh-treated MASH mice and decreased in LSECs from 9-ING-41-treated MASH mice (Fig. 6G and Fig. S7C). However, pharmacological GSK3 inhibition did not significantly reduce the migration of bone marrow-derived monocytes isolated from mice with MASH (Fig. 6H) or

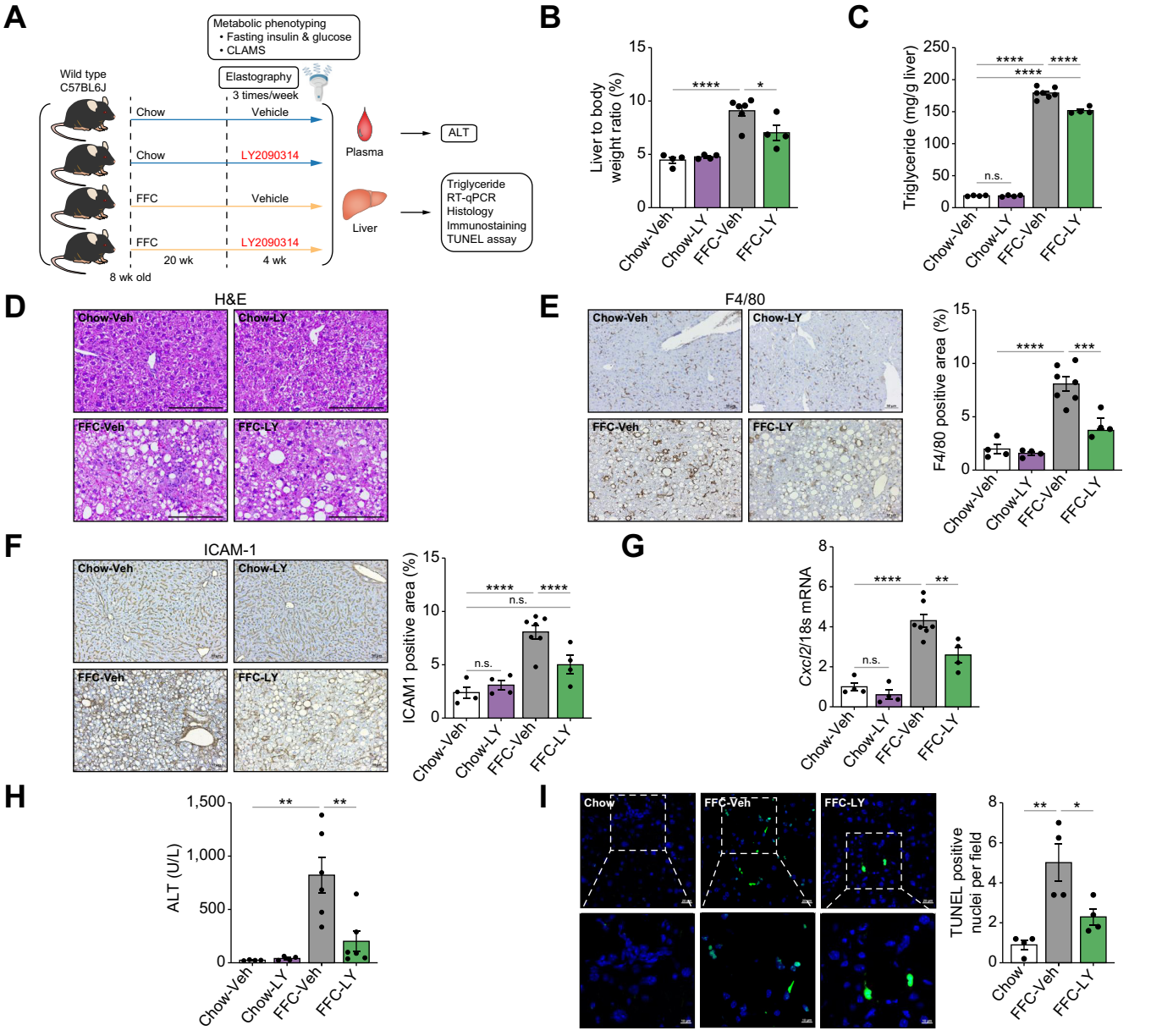

Fig. 4. Glycogen synthase kinase (GSK)-3 inhibition ameliorates liver injury and inflammation in fat, fructose, and cholesterol (FFC) diet-induced murine metabolic dysfunction-associated steatohepatitis (MASH). Wild-type (WT) C57BL/6J mice were fed either a chow or FFC diet for 24 weeks and treated with either vehicle (Veh) or the GSK3 inhibitor LY2090314 (LY) intraperitoneally 10 mg/kg three times per week for 4 weeks. (A) Schematic of the feeding experiment. (B) Liver-to-body weight ratio. (C) Liver triglyceride content. (D) Representative images of H&E staining of the liver sections. (E) Representative images of F4/80 immunostaining of the liver sections (left). F4/80-positive areas were quantified in five random 10 × microscopic fields and averaged for each animal (right). (F) Representative images of intracellular adhesion molecule 1 (ICAM-1) immunostaining in liver sections (left). ICAM-1-positive area is quantified (right). (G) Hepatic mRNA expression of C-X-C motif chemokine ligand 2 (*Cxcl2*). (H) Plasma alanine aminotransferase (ALT) level. (I) Representative images of terminal deoxynucleotidyl transferase dUTP nick-end labeling (TUNEL) staining of the liver sections (left). Quantification of TUNEL-positive cells (right). The marked boxes in the top images indicate the magnified images at the bottom. Bar graphs represent the mean ± SEM; $^{*}p$ <0.05, $^{**}p$ <0.01, $^{***}p$ <0.001, $^{****}p$ <0.0001, ns, non-significant (one-way ANOVA with Bonferroni's multiple comparison; n = 4–7). Scale bars: 10 μm (I, insets), 20 μm (I), 50 μm (E,F), 100 μm (D).

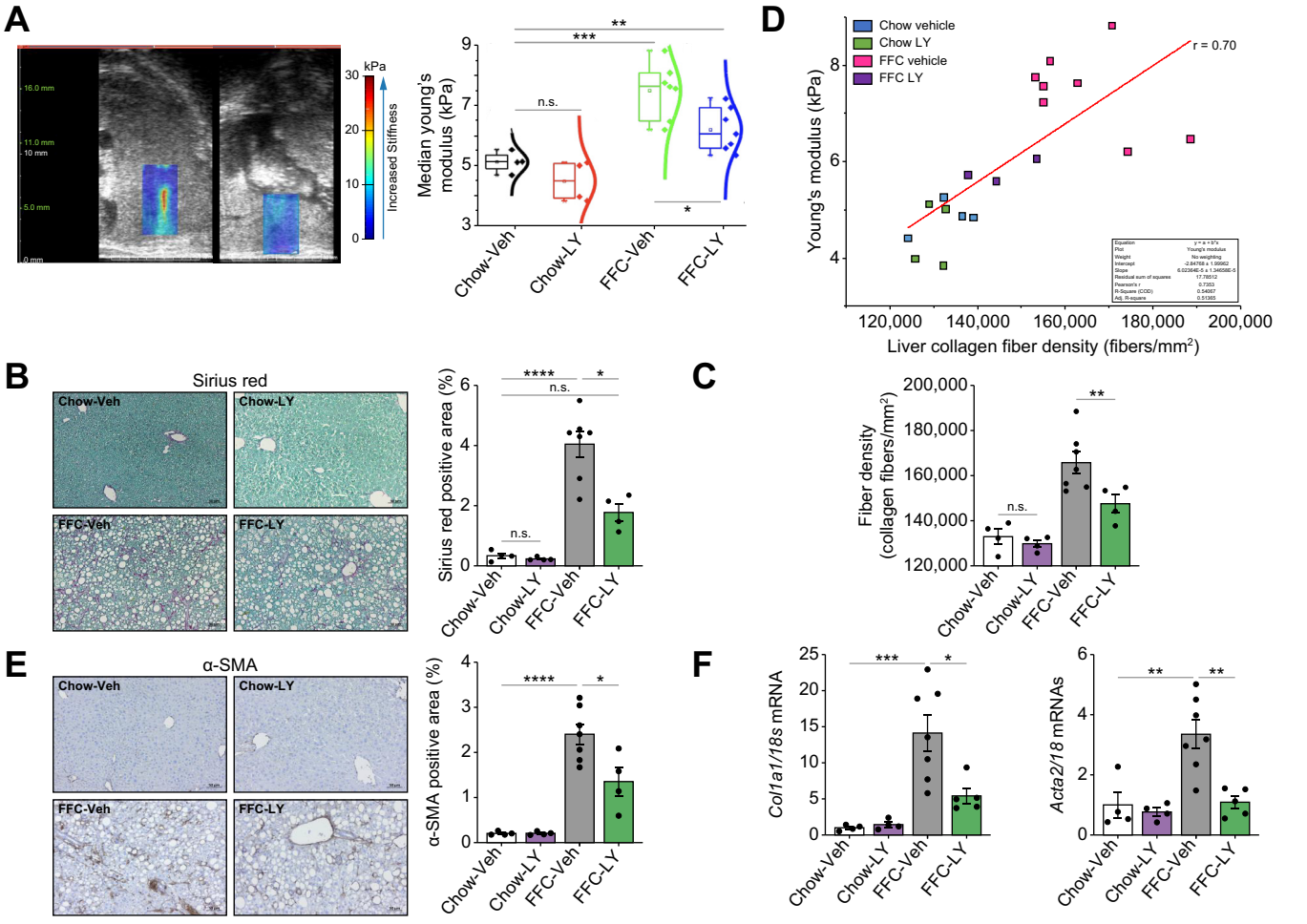

Fig. 5. Glycogen synthase kinase (GSK)-3 inhibition by LY2090314 (LY)-ameliorated liver fibrosis in diet-induced murine metabolic dysfunction-associated steatohepatitis (MASH). (A) Ultrasound images of the liver using shear wave elastography segmentation overlay. Median Young's modulus (kPa) of the vehicle (Veh) and LY-treated mice fed chow or a fat, fructose, and cholesterol (FFC) diet. (B) Representative images of Sirius Red staining of liver sections (left). Sirius Red-positive areas were quantified in five random 10 × microscopic fields and averaged for each animal (right). (C) *Ex vivo* validation of collagen fiber density after the final time point using CT-FIRE (left). (D) Correlation between *in vivo* ultrasound and *ex vivo* CT-FIRE measurements of liver fibrosis pooled across all groups. Pearson's r correlation = 0.7 (right). (E) Representative images of alpha-smooth muscle actin (α-SMA) immunostaining (left) and quantification (right) of liver sections. (F) α-SMA and Collagen1α1 mRNA expression levels. Bar graphs represent mean ± SEM; **p* <0.05, ***p* <0.01, ****p* <0.001, *****p* <0.0001, ns, non-significant (one-way ANOVA with Bonferroni's multiple comparison; n = 4–7). Scale bars: 50 μm (B,E).

subjected to the chemokine CCL2 (Fig. S8), suggesting a minor direct effect of GSK3 inhibition on monocyte recruitment.

To further examine the contribution of the different immune cells to the protective effect of GSK3 inhibition in MASH, we used mass cytometry by time of flight (CyTOF) using the Fluidigm Helios System, which allows comprehensive profiling of intrahepatic leukocyte (IHL) subpopulations based on multiple cell markers. Thirty-one clusters were obtained (Fig. 7A) on isolated IHLs from mice from the different experimental groups based on the intensities of 32 different cell surface markers and two cytosolic markers (S100A8 and MPO) (Fig. 7A and B; Tables S1 and S2, and Fig. S9), which allowed comprehensive profiling of the phenotype, differentiation, and function of the intrahepatic subpopulations of innate and adaptive immune cells. t-Distributed stochastic neighbor embedding (tSNE) plots of each experimental group were analyzed, with red indicating high-frequency categorization of cells to a cluster and blue indicating low frequency (Fig. 7C). Our data indicate that the cell percentages of clusters 31 and 6, representing monocyte-derived dendritic cells (MoDCs) (Fig. 7D and E), and cluster 9, comprising proinflammatory monocyte-derived macrophages (MoMFs) (Fig. 7F), increased with the CDHFD diet and decreased with 9-ING-41 treatment. However, 9-ING-41 treatment in CDHFD-fed mice did not significantly alter the percentage of other intrahepatic immune cell subpopulations in the remaining clusters (Fig. S10), further confirming that GSK3 inhibition reduces circulating myeloid cell infiltration and proinflammatory differentiation in the MASH liver.

To further study the effects of GSK3 inhibitor on liver fibrosis in MASH, we performed Sirius Red staining, which showed a reduction in Sirius Red-positive area in the CDHFD-fed 9-ING-41-treated mice compared with Veh-treated mice on the same diet (Fig. 8A). Likewise, these findings were replicated with immunostaining for α-SMA (Fig. 8B), and measurement of *Col1a1* mRNA expression (Fig. 8C), indicating a protective effect of 9-

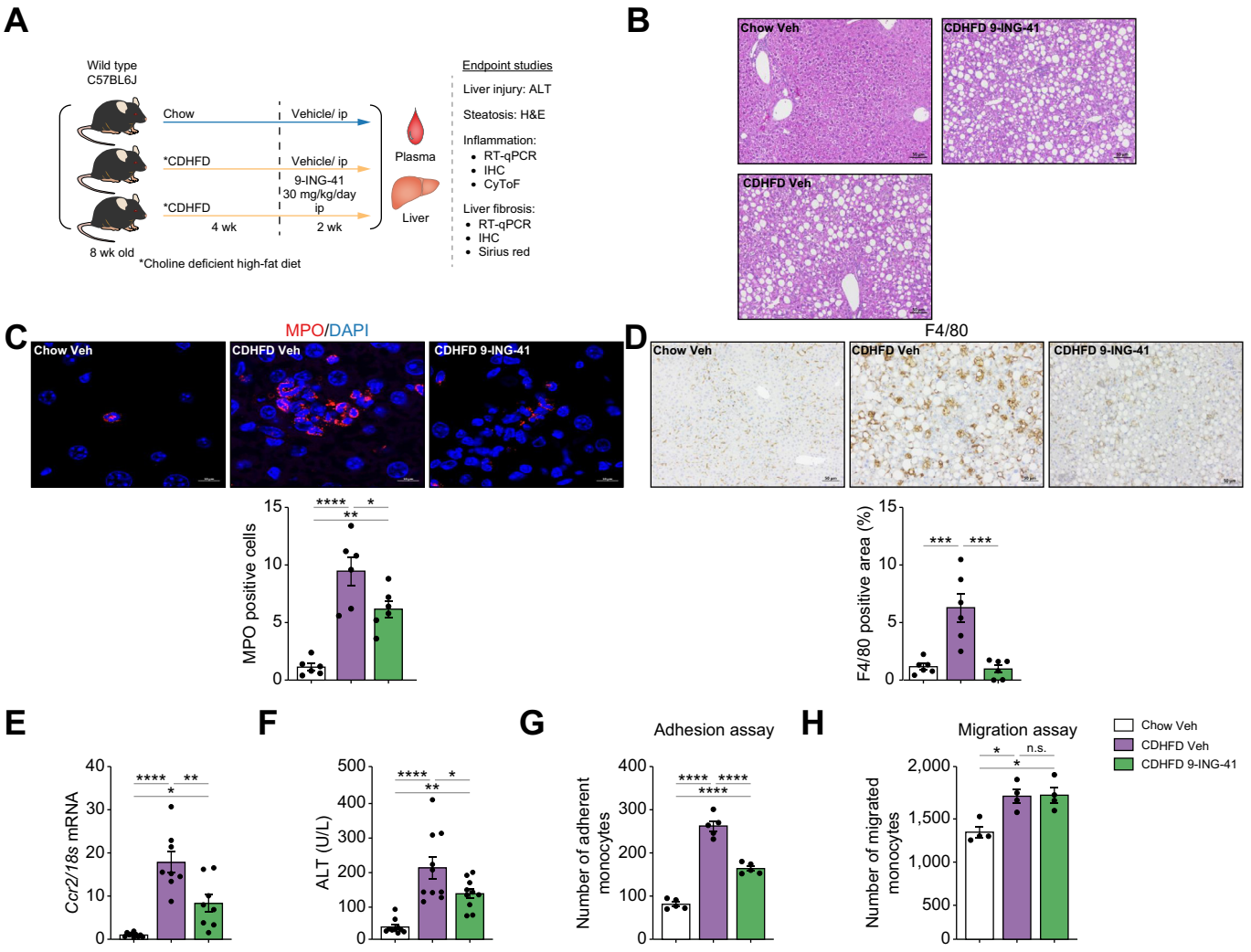

Fig. 6. Glycogen synthase kinase (GSK)-3 inhibition with elraglusib improves liver injury and inflammation in choline-deficient high-fat diet (CDHFD)-induced murine metabolic dysfunction-associated steatohepatitis (MASH). Eight-week-old wild-type (WT) C57BL/6J mice were fed either a chow diet or CDHFD for 6 weeks and treated with either vehicle (Veh) or the GSK3 inhibitor 9-ING-41 (intraperitoneally 30 mg/kg daily for 2 weeks). (A) Schematic of the feeding experiment. (B) Representative images of H&E staining of the liver sections. (C) Myeloperoxidase (MPO) immunofluorescence staining (red) Nuclei were stained with DAPI (blue). Images are shown at a 63 × magnification. (D) F4/80 immunostaining of liver sections (left). F4/80-positive areas were quantified in five random 10 × microscopic fields and averaged for each animal (right). (E) Hepatic mRNA expression levels of *Ccr2*. (F) Plasma alanine aminotransferase (ALT) levels (n = 5–10). Quantification of (G) monocytes adherent to liver sinusoidal endothelial cells (LSECs) (n = 5), (H) and migrating monocytes (n = 3) in the different experimental groups. Bar graphs represent mean ± SEM; *p <0.05, **p <0.01, ***p <0.001, ****p <0.0001, ns, non-significant (one-way ANOVA with Bonferroni's multiple comparison). Scale bars: 10 μm (C), 50 μm (B,D).

ING-41 against MASH-associated liver fibrosis. Taken together, these findings suggest that pharmacological inhibition of GSK3 by 9-ING-41 in CDHFD-induced murine MASH ameliorates liver inflammation, injury, and fibrosis.

Discussion

The current study provides insight into the role of GSK3 in lipotoxicity-induced LSEC endotheliopathy in MASH. Herein, we demonstrate that: (i) in LSECs isolated from mice with diet-induced MASH, leukocyte TEM and focal adhesion are among the major altered pathways in differentially expressed proteomics and transcriptomics; (ii) based on kinome profiling, GSK3 is the central hub kinase associated with MASH pathogenesis in LSECs; (iii) GSK3 drives the toxic lipid-induced proinflammatory phenotype in LSECs; and (iv) pharmacological inhibition of GSK3, using two distinct pharmacological inhibitors and two different mouse models of MASH, ameliorates liver inflammation, injury, and fibrosis mainly by reducing myeloid cell infiltration and proinflammatory differentiation in the MASH liver.

Given that protein phosphorylation is central to dynamic biological processes, including metabolic and immune responses, multiple liver phosphoproteomic studies have shed light on the key mediators of metabolic liver diseases. For example, pathway analysis of the liver phosphoproteome of patients with MASH and simple steatosis identified carbohydrate metabolism as a significant biological process relevant to MASH progression.[34] In another liver phosphoproteomics study using a murine model of alcohol-associated liver disease, the apoptosis signal-regulating kinase 1 (ASK1)–p38 axis was identified as a downstream target of the pro-necroptotic protein receptor-interaction protein kinase 3 (RIP3).[35] These whole-liver phosphoproteomic studies

likely reflect signaling alterations in hepatocytes. To the best of our knowledge, the current study is the first to examine the phosphoproteome of LSECs, the most abundant and highly immunogenic cell population among non-parenchymal liver cells. Notably, none of the previous liver phosphoproteomic studies detected GSK3 as a signaling hub, which implies that an LSEC-specific kinase-driven signaling network exists in the context of metabolic perturbations in the liver. Moreover, a previous study reported that the phosphorylation levels of GSK3 in adipose tissue are one of the predictors of advanced liver fibrosis in patients with metabolic dysfunction-associated steatotic liver disease (MASLD).[36] Taken together, these studies suggest that altered GSK3 activation is a common driver in the pathophysiology of metabolic syndrome (MS) across multiple organs.

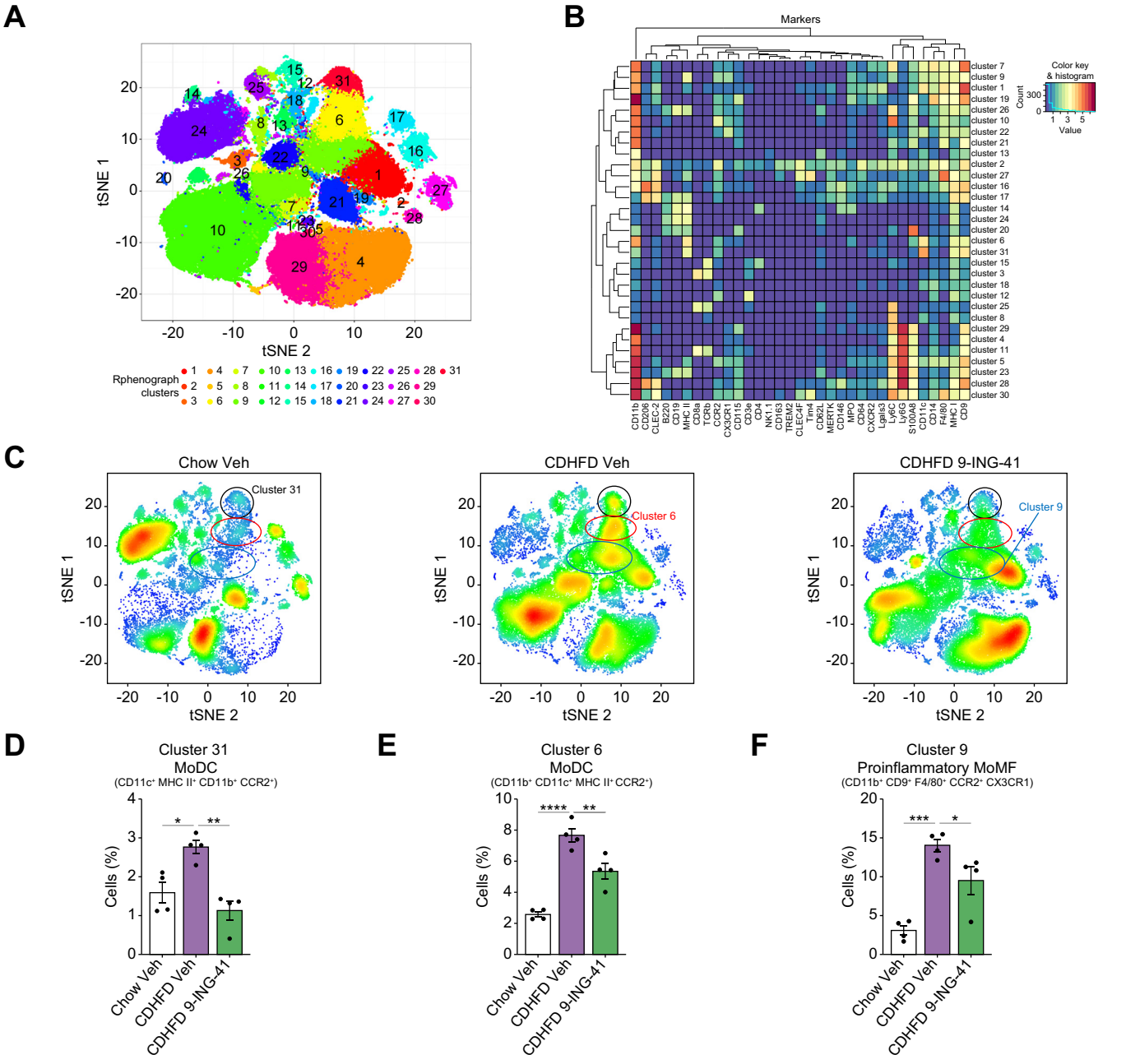

Fig. 7. Glycogen synthase kinase (GSK)-3 inhibition with elraglusib attenuates the recruitment of proinflammatory myeloid cells in the liver of choline-deficient high-fat diet (CDHFD)-fed mice. Cytometry by time of flight (CyTOF) was performed on intrahepatic leukocytes (IHLs) of chow-fed mice and CDHFD-fed mice treated with the GSK3 inhibitor elraglusib (9-ING-41). (A) Thirty-one unique clusters were defined by a panel of 32 cell-surface markers, including CD45 and two intracellular markers (myeloperoxidase [MPO] and S100A8) using the Rphenograph clustering algorithm and visualized on a tSNE plot. (B) Heatmap demonstrating the distribution and relative intensity of the markers used in clustering analysis. (C) Representative tSNE plots of each experimental group. Red indicates high-frequency categorization of cells into a cluster, and blue indicates low frequency. Clusters 31 (D) and 6 (E) are consistent with monocyte-derived dendritic cells (MoDCs), whereas cluster 9 (F) is consistent with proinflammatory monocyte-derived macrophages (MoMFs). Bar graphs represent the mean ± SEM; *p <0.05, **p <0.01, ***p <0.001, ****p <0.0001 (one-way ANOVA with Bonferroni's multiple comparison; n = 4). tSNE, t-distributed stochastic neighbor embedding.

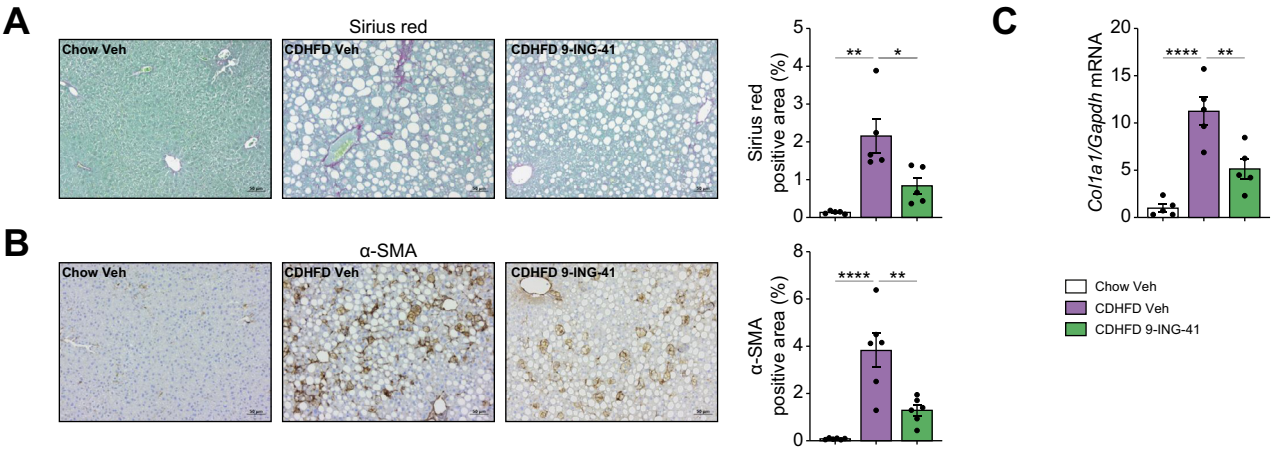

Fig. 8. Elraglusib (9-ING-41) treatment in choline-deficient high-fat diet (CDHFD)-fed mice attenuates liver fibrosis. (A) Representative images of Sirius Red staining of liver sections (left). Sirius Red-positive areas were quantified (right). (B) Representative images of α-SMA immunostaining of the liver sections (left). α-SMA-positive areas were quantified (right). (C) Hepatic mRNA expression levels of collagen 1α1 were assessed. Bar graphs represent the mean ± SEM; *p <0.05, **p <0.01, ****p <0.0001 (one-way ANOVA with Bonferroni's multiple comparison) (n = 5 or 6). Scale bars: 50 μm (A,B).

Our study identified *ICAM1* and *CXCL2* as downstream targets of GSK3 in LSECs; interestingly, both ICAM-1 and CXCL2 are prerequisites for circulating leukocyte TEM and recruitment to inflamed tissue.[37,38] Moreover, pathway analysis of the multi-omics data sets on LSECs from murine MASH identified focal adhesion and leukocyte TEM as significant biological processes in MASH progression, further implicating *ICAM1* and *CXCL2* in MASH pathogenesis. Likewise, we identified a GSK3-dependent increase in VE-cadherin phosphorylation in LSECs under lipotoxic stress, promoting immune cell TEM. However, VE-cadherin phosphorylation and internalization can also modulate endothelial growth factor receptor function, cell survival through the PI3K/AKT signaling pathway, cell proliferation via the ERK/MAPK pathway, and cell migration via the GTPase RhoA pathway.[39] Hence, these pathways are potentially implicated in lipotoxic endotheliopathy.

ICAM-1 is an adhesion molecule of the Ig superfamily and is predominantly expressed in endothelial cells. It has been shown previously that toxic lipids induce aberrant expression of the other Ig superfamily member, vascular cell adhesion molecule 1 (VCAM1), in LSECs, and that endothelial cell-specific genetic deletion or pharmacological inhibition of VCAM1 ameliorates murine MASH.[7] In addition, CXCL2, along with other CXCL chemokines, has been implicated in leukocyte chemotaxis via its cognate binding interaction with CXC motif chemokine receptor 2 (CXCR2), a typical G-protein-coupled receptor.[40] Increased levels of CXCL2 have been observed in the serum of individuals with obesity.[41] CXCL2 shares 90% amino acid sequence similarity with the related chemokine CXCL1, the biological function of which has been studied extensively.[40,42] It is intriguing that, in our NanoString-based gene expression analysis, *CXCL2*, but not *CXCL1*, was among the 'lipotoxic stress-dependent' and 'GSK3-dependent' genes, suggesting the different transcriptional regulation mechanisms between these two molecules. Furthermore, the expression of *CXCL2* was reduced by the GSK3 inhibitor LY in murine MASH, suggesting that LSEC GSK3 signaling in MASH is also implicated in chemotaxis.

Although the two isoforms of GSK3 (α and β) share 85% amino acid sequence homology,[43] whole-body GSK3β-knockout mice are embryonically lethal, whereas GSK3α-knockout mice are viable, indicating that these two isoforms have non-redundant functions.[44,45] Recently, pharmacological inhibition of GSK3 or endothelial cell-specific deletion of GSK3β was reported to reduce atherosclerotic calcification in *Apoe*$^{-/-}$ Western diet-fed mice.[46] In another murine atherosclerosis model, deletion of endothelial GSK3α, but not GSK3β, attenuated atherosclerosis, which was associated with reduced endothelial adhesion molecule expression and monocyte recruitment to the vascular wall.[47] Despite several similarities, one of the differences between this and the current study is that GSK3α-deleted endothelial cells had decreased expression of VCAM1 *in vivo*, whereas, in the current study, GSK3 inhibition reduced the expression of ICAM-1 *in vitro* and *in vivo*. This discrepancy might be secondary to the differences between vascular endothelial cells and LSECs, which are specialized fenestrated endothelial cells. Furthermore, GSK3 inhibitors suppress the kinase activity of both GSK3α and GSK3β because of the extremely high amino acid homology in the kinase domain of these two isoforms.[48] Taken together, these studies suggest that GSK3 inhibition would have a beneficial effect on extrahepatic vascular manifestations of MS, further supporting the involvement of GSK3 in endothelial inflammation. Ongoing experiments are exploring the distinct role of GSK3β *vs.* GSK3α in LSECs *vs.* hepatocytes in murine MASH, and their role in disease development and progression, which are beyond the scope of the current manuscript.

Nevertheless, our *in vivo* studies demonstrated that GSK3 inhibitors are well tolerated and elicit robust improvements in liver inflammation, injury, and fibrosis in diet-induced murine MASH, which, from a clinical perspective, might be as informative as findings obtained from genetically engineered mouse models. In addition, GSK3 inhibitors have been safely and effectively used for decades in mood disorders[49] and, therefore, could be repurposed for MASH therapy.

Collectively, our study implicates GSK3 in the proinflammatory phenotype of LSECs in MASH and provides preclinical data to support targeting GSK3 as a novel anti-inflammatory and antifibrotic therapeutic approach in human MASH.

Abbreviations

α-SMA, alpha-smooth muscle actin; ALT, alanine aminotransferase; ASK1, apoptosis signal-regulating kinase 1; CDHFD, choline-deficient high fat diet; CXCL2, C-X-C motif chemokine ligand 2; CXCR2, CXC motif chemokine receptor 2; CyTOF, cytometry by time of flight; FAK, focal adhesion kinase; FFA, free fatty acid; FFC, fat, fructose and cholesterol; GAPDH, glyceraldehyde-3-phosphate dehydrogenase; GS, glycogen synthase; GSK3, glycogen synthase kinase 3; HOMA-IR, Homeostatic Model Assessment for Insulin Resistance; ICAM-1, intracellular adhesion molecule 1; IHL, intrahepatic leukocyte; KEGG, Kyoto Encyclopedia of Genes and Genomes; LPC, lysophosphatidylcholine; LSEC, liver sinusoidal endothelial cell; LY, LY2090314; MASH, metabolic dysfunction associated steatohepatitis; MASLD, metabolic dysfunction-associated steatotic liver disease; MoDC, monocyte-derived dendritic cells; MoMF, monocyte-derived macrophage; MPO, myeloperoxidase; MS, metabolic syndrome; NAS, NASH Clinical Research Network Scoring System; p-GS, phosphorylated glycogen synthase; PA, palmitate; qPCR, quantitative PCR; RIP3, receptor-interacting protein kinase 3; RNA-seq, RNA-sequencing; siRNA, small interfering RNA; TEM, transendothelial migration; TNF-α, tumor necrosis factor-α; TSEC, transformed mouse liver sinusoidal endothelial cell; tSNE, t-distributed stochastic neighbor embedding; TUNEL, terminal deoxynucleotidyl transferase dUTP nick-end labeling; VCAM1, vascular cell adhesion molecule 1; VE-cadherin, vascular endothelial cadherin; Veh, vehicle; WT, wild-type; YM, Young's modulus.

Financial support

The research reported in this publication was supported by the Mayo Foundation and the National Institute of Diabetes and Digestive and Kidney Diseases (NIDDK) of the National Institutes of Health (NIH) under Award R01DK122948 to SHI, NIH shared instruments grant (S10OD028633), and P30DK084567 to the Mayo Clinic Center for Cell Signaling in Gastroenterology, and JSPS Overseas Research Fellowships to KF Support was also provided to PH by NIDDK NIH under Award R01DK130884; to HL by the Mayo Clinic Cancer Center (P30CA015083), David F. and Margaret T. Grohne Cancer Immunology and Immunotherapy Program, Mayo Center for Biomedical Discovery, Center for Individualized Medicine, and Eric & Wendy Schmidt Fund for AI Research & Innovation; to AOB by NIDDK NIH under Award K01DK124358; to CRS from the Zell Family Foundation; to MFR from R43DK126607; and to CM by an Innovation grant ADL0048, sponsored by the Department of Laboratory Medicine and Pathology Translational Research, Innovation and Test Development Office (TRITDO) and the Center for Individualized Medicine (CIM) at the Mayo Clinic.

Conflicts of interest

The authors declare no conflicts of interest.

Please refer to the accompanying ICMJE disclosure forms for further details.

Authors' contributions

Concept formulation: SHI. Designed research studies: MK, QG, KF, SHI. Conducted experiments: MK, QG, KF, HSKL, KW, LVP, SI. Acquired data: MK, QG, KF, HSKL, HH, SI. Analyzed data: MK, QG, KF, CC, HSKL, HH, MR, CS, KP, HL, SI, SHI. Designed and implemented the AI algorithm for liver zonation and steatosis quantification: CM. Designed software for automatic quantification of steatosis on digitized slides: IK, Y–KN. Provided materials: AM, AOB, PH. Drafted manuscript: MK, QG, KF, CC, SHI. Revised manuscript: CC, AM, AOB, PH, HH, MR, CS, KP, HL, SHI.

Data availability statement

RNA-seq data on isolated mouse LSECs were deposited in the Gene Expression Omnibus database (GSE164006); proteomics and phosphoproteomics data on isolated mouse LSECs were deposited in the ProteomeXchange Consortium via the PRIDE partner repository (PXD048073).

Acknowledgements

The authors thank Gregory J. Gores for his scientific insight and acknowledge the assistance of the Proteomic Core at Mayo Clinic led by Akhilesh Pandey.

Supplementary data

Supplementary data to this article can be found online at https://doi.org/10.1016/j.jhepr.2024.101073.

References

Author names in bold designate shared co-first authorship

[1] Younossi ZM. Non-alcoholic fatty liver disease – a global public health perspective. J Hepatol 2019;70:531–544.
[2] Neuschwander-Tetri BA. Hepatic lipotoxicity and the pathogenesis of nonalcoholic steatohepatitis: the central role of nontriglyceride fatty acid metabolites. Hepatology 2010;52:774–788.
[3] Friedman SL, Neuschwander-Tetri BA, Rinella M, et al. Mechanisms of NAFLD development and therapeutic strategies. Nat Med 2018;24:908–922.
[4] McConnell MJ, Kostallari E, Ibrahim SH, et al. The evolving role of liver sinusoidal endothelial cells in liver health and disease. Hepatology 2023;78:649–669.
[5] Ibrahim SH. Sinusoidal endotheliopathy in nonalcoholic steatohepatitis: therapeutic implications. Am J Physiol Gastrointest Liver Physiol 2021;321:G67–G74.
[6] Furuta K, Tang X, Islam S, et al. Endotheliopathy in the metabolic syndrome: mechanisms and clinical implications. Pharmacol Ther 2023;244:108372.
[7] Furuta K, Guo Q, Pavelko KD, et al. Lipid-induced endothelial vascular cell adhesion molecule 1 promotes nonalcoholic steatohepatitis pathogenesis. J Clin Invest 2021;131:e143690.
[8] Miyachi Y, Tsuchiya K, Komiya C, et al. Roles for cell-cell adhesion and contact in obesity-induced hepatic myeloid cell accumulation and glucose intolerance. Cell Rep 2017;18:2766–2779.
[9] **Guo Q**, **Furuta K**, Islam S, et al. Liver sinusoidal endothelial cell expressed vascular cell adhesion molecule 1 promotes liver fibrosis. Front Immunol 2022;13:983255.
[10] Ritz T, Krenkel O, Tacke F. Dynamic plasticity of macrophage functions in diseased liver. Cell Immunol 2018;330:175–182.
[11] **Krenkel O**, **Hundertmark J**, Abdallah AT, et al. Myeloid cells in liver and bone marrow acquire a functionally distinct inflammatory phenotype during obesity-related steatohepatitis. Gut 2020;69:551–563.
[12] **McNamara HA**, **Cockburn IA**. The three rs: recruitment, retention and residence of leukocytes in the liver. Clin Trans Immunol 2016;5:e123.
[13] Miyao M, Kotani H, Ishida T, et al. Pivotal role of liver sinusoidal endothelial cells in NAFLD/NASH progression. Lab Invest 2015;95:1130–1144.
[14] **Guo Q**, **Furuta K**, Lucien F, et al. Integrin beta1-enriched extracellular vesicles mediate monocyte adhesion and promote liver inflammation in murine NASH. J Hepatol 2019;71:1193–1205.
[15] Muller WA. Transendothelial migration: unifying principles from the endothelial perspective. Immunol Rev 2016;273:61–75.
[16] Shetty S, Lalor PF, Adams DH. Liver sinusoidal endothelial cells – gatekeepers of hepatic immunity. Nat Rev Gastroenterol Hepatol 2018;15:555–567.
[17] Beurel E, Grieco SF, Jope RS. Glycogen synthase kinase-3 (GSK3): regulation, actions, and diseases. Pharmacol Ther 2015;148:114–131.
[18] Jeffers A, Qin W, Owens S, et al. Glycogen synthase kinase-3beta inhibition with 9-ING-41 attenuates the progression of pulmonary fibrosis. Sci Rep 2019;9:18925.
[19] **Ramirez SH**, **Fan S**, Zhang M, et al. Inhibition of glycogen synthase kinase 3beta (GSK3beta) decreases inflammatory responses in brain endothelial cells. Am J Pathol 2010;176:881–892.
[20] **Yi L**, **Huang X**, Guo F, et al. GSK-3beta-dependent activation of GEF-H1/ROCK signaling promotes LPS-induced lung vascular endothelial barrier dysfunction and acute lung injury. Front Cel Infect Microbiol 2017;7:357.
[21] Nakamura M, Liu T, Husain S, et al. Glycogen synthase kinase-3alpha promotes fatty acid uptake and lipotoxic cardiomyopathy. Cell Metab 2019;29:1119–1134.

[22] Gutierrez Sanchez LH, Tomita K, Guo Q, et al. Perinatal nutritional reprogramming of the epigenome promotes subsequent development of nonalcoholic steatohepatitis. Hepatol Commun 2018;2:1493–1512.
[23] Furuta K, Guo Q, Hirsova P, et al. Emerging roles of liver sinusoidal endothelial cells in nonalcoholic steatohepatitis. Biology 2020;9:395.
[24] **Lachmann A**, **Ma'ayan A**. KEA: kinase enrichment analysis. Bioinformatics 2009;25:684–686.
[25] de Almeida IT, Cortez-Pinto H, Fidalgo G, et al. Plasma total and free fatty acids composition in human non-alcoholic steatohepatitis. Clin Nutr 2002;21:219–223.
[26] Hughes K, Nikolakaki E, Plyte SE, et al. Modulation of the glycogen synthase kinase-3 family by tyrosine phosphorylation. EMBO J 1993;12:803–808.
[27] Kakisaka K, Cazanave SC, Fingas CD, et al. Mechanisms of lysophosphatidylcholine-induced hepatocyte lipoapoptosis. Am J Physiol Gastrointest Liver Physiol 2012;302:G77–G84.
[28] Kolhe R, Ghilzai U, Mondal AK, et al. Nanostring-based identification of the gene expression profile in trigger finger samples. Healthcare (Basel) 2021;9:1592.
[29] Wang W, Lollis EM, Bordeleau F, et al. Matrix stiffness regulates vascular integrity through focal adhesion kinase activity. FASEB J 2019;33:1199–1208.
[30] Sullivan DP, Dalal PJ, Jaulin F, et al. Endothelial IQGAP1 regulates leukocyte transmigration by directing the LBRC to the site of diapedesis. J Exp Med 2019;216:2582–2601.
[31] Gray JE, Infante JR, Brail LH, et al. A first-in-human phase I dose-escalation, pharmacokinetic, and pharmacodynamic evaluation of intravenous LY2090314, a glycogen synthase kinase 3 inhibitor, administered in combination with pemetrexed and carboplatin. Invest New Drugs 2015;33:1187–1196.
[32] Ekstedt M, Hagström H, Nasr P, et al. Fibrosis stage is the strongest predictor for disease-specific mortality in NAFLD after up to 33 years of follow-up. Hepatology 2015;61:1547–1554.
[33] Matsumoto M, Hada N, Sakamaki Y, et al. An improved mouse model that rapidly develops fibrosis in non-alcoholic steatohepatitis. Int J Exp Pathol 2013;94:93–103.
[34] Wattacheril J, Rose KL, Hill S, et al. Non-alcoholic fatty liver disease phosphoproteomics: a functional piece of the precision puzzle. Hepatol Res 2017;47:1469–1483.
[35] Singh V, Huang E, Pathak V, et al. Phosphoproteomics identifies pathways underlying the role of receptor-interaction protein kinase 3 in alcohol-associated liver disease and uncovers apoptosis signal-regulating kinase 1 as a target. Hepatol Commun 2022;6:2022–2041.
[36] Younossi ZM, Baranova A, Stepanova M, et al. Phosphoproteomic biomarkers predicting histologic nonalcoholic steatohepatitis and fibrosis. J Proteome Res 2010;9:3218–3224.
[37] Girbl T, Lenn T, Perez L, et al. Distinct compartmentalization of the chemokines CXCL1 and CXCL2 and the atypical receptor ACKR1 determine discrete stages of neutrophil diapedesis. Immunity 2018;49:1062–1076.
[38] Arts JJG, Mahlandt EK, Gronloh MLB, et al. Endothelial junctional membrane protrusions serve as hotspots for neutrophil transmigration. Elife 2021;10:e66074.
[39] Nan W, He Y, Wang S, et al. Molecular mechanism of VE-cadherin in regulating endothelial cell behaviour during angiogenesis. Front Physiol 2023;14:1234104.
[40] Cheng Y, Ma XL, Wei YQ, et al. Potential roles and targeted therapy of the CXCLs/CXCR2 axis in cancer and inflammatory diseases. Biochim Biophys Acta Rev Cancer 2019;1871:289–312.
[41] Rouault C, Pellegrinelli V, Schilch R, et al. Roles of chemokine ligand-2 (CXCL2) and neutrophils in influencing endothelial cell function and inflammation of human adipose tissue. Endocrinology 2013;154:1069–1079.
[42] Vries MH, Wagenaar A, Verbruggen SE, et al. CXCL1 promotes arteriogenesis through enhanced monocyte recruitment into the peri-collateral space. Angiogenesis 2015;18:163–171.
[43] Woodgett JR. Molecular cloning and expression of glycogen synthase kinase-3/factor A. EMBO J 1990;9:2431–2438.
[44] Hoeflich KP, Luo J, Rubie EA, et al. Requirement for glycogen synthase kinase-3beta in cell survival and NF-kappaB activation. Nature 2000;406:86–90.
[45] MacAulay K, Doble BW, Patel S, et al. Glycogen synthase kinase 3alpha-specific regulation of murine hepatic glycogen metabolism. Cel Metab 2007;6:329–337.
[46] **Cai X**, **Zhao Y**, Yang Y, et al. GSK3beta inhibition ameliorates atherosclerotic calcification. Int J Mol Sci 2023;24:11638.
[47] **Mastrogiacomo L**, **Werstuck GH**. Investigating the role of endothelial glycogen synthase kinase3alpha/beta in atherogenesis in low density lipoprotein receptor knockout mice. Int J Mol Sci 2022;23:14780.
[48] Kaidanovich-Beilin O, Woodgett JR. GSK-3: functional insights from cell biology and animal models. Front Mol Neurosci 2011;4:40.
[49] Jope RS. Glycogen synthase kinase-3 in the etiology and treatment of mood disorders. Front Mol Neurosci 2011;4:16.

Journal of Hepatology, Volume *6*

Supplemental information

Glycogen synthase kinase 3 activity enhances liver inflammation in MASH

Mireille Khoury, Qianqian Guo, Kunimaro Furuta, Cristina Correia, Chady Meroueh, Hyun Se Kim Lee, Khaled Warasnhe, Lucía Valenzuela-Pérez, Andrew P. Mazar, Iljung Kim, Yung-Kyun Noh, Heather Holmes, Michael F. Romero, Caroline R. Sussman, Kevin D. Pavelko, Shahidul Islam, Adebowale O. Bamidele, Petra Hirsova, Hu Li, and Samar H. Ibrahim

Glycogen synthase kinase 3 activity enhances liver inflammation in MASH

Mireille Khoury, Qianqian Guo, Kunimaro Furuta, Cristina Correia, Chady Meroueh, Hyun Se Kim Lee, Khaled Warasnhe, Lucía Valenzuela Pérez, Andrew P. Mazar, Iljung Kim, Yung-Kyun Noh, Heather Holmes, Michael F. Romero, Caroline R. Sussman, Kevin D. Pavelko, Shahidul Islam, Adebowale O. Bamidele, Petra Hirsova, Hu Li, Samar H. Ibrahim

Table of contents

Materials and methods

Materials. Palmitate (PA) (P0500) was obtained from Sigma-Aldrich (St. Louis, MO, USA). Louis, MO). Primary antibodies employed for the studies include anti-alpha smooth muscle actin (α-SMA) (ab124964) from Abcam (Cambridge, MA), anti-GAPDH (MAB374) from Millipore Sigma, anti-β-actin (sc-47778) from Santa Cruz Biotechnologies (Santa Cruz, CA), anti-H/M Myeloperoxidase (MPO) (#AF3667), anti-ICAM-1 (#AF796SP) from R&D systems, anti-GSK3β (D5C5Z) (#12456), anti-phospho-β-catenin (Ser33/37/Thr41) (#9561), anti-glycogen synthase (3893S), anti-phospho glycogen synthase (Ser641) (#3891S), anti-VE-Cadherin (#2158S), anti-FAK (#3285S) and anti F4/80 (#70076S) from Cell Signaling Technology (Danvers, MA), and anti-phospo-GSK3α/β (Try216/Try279) (#44-604G), anti-phospho FAK (#44-624G), anti-phospho VE-Cadherin (Tyr658) (#44-1144G) from Thermo Fisher Scientific (Waltham, MA). Recombinant human TNF-α (210-TA) and TGF-β1 (7754-BH) were obtained from R&D Systems. LY2090314 (S7063) was purchased from Selleck Chemicals, LLC (Houston, TX, USA). Elraglusib (9-ING-41) was gifted by Acuate Therapeutics Inc. (Fort Worth, TX, USA).

Cells. Primary human liver sinusoidal endothelial cells (LSEC) were purchased from ScienCell Research Laboratories (San Diego, CA). Primary mouse LSEC were isolated using collagenase perfusion and immunomagnetic selection as previously described[1, 2]. Briefly, the liver was digested with collagenase infused via the portal vein, and the obtained cell suspensions were centrifuged at 50 × g for 2 min to remove the hepatocytes. The supernatant, which included non-parenchymal cells, was subjected to LSEC isolation using CD146 MicroBeads (Miltenyi Biotec, Bergisch Gladbach, Germany) following the manufacturer's instructions. Primary human and mouse LSEC and immortalized mouse LSEC cell lines (TSEC) were cultured in Endothelial Cell Growth Medium (211-500, Sigma) consisting of 5% fetal bovine serum (FBS) and 1% endothelial

cell growth supplement supplemented with 1% primocin (InvivoGen, San Diego, CA). TSEC were generated by Dr. Shah's lab from LSEC isolated from mouse liver using CD31-based immunomagnetic separation, immortalized with SV40 large T-antigen, and subcloned based on their ability to endocytose acetylated low-density lipoprotein. The resulting cell line, transformed sinusoidal endothelial cells (TSEC), maintains an endothelial phenotype as well as some LSEC-specific features [3]. The human monocytic cell line THP-1, derived from a 1-year-old boy with acute monocytic leukemia, was purchased from ATCC (Rockville, MD, USA) and cultured in RPMI-1640 medium supplemented with 10% fetal bovine serum. All the cell cultures were maintained at 37°C in a humidified atmosphere containing 5% CO_2. GSK3β knockdown in LSEC was performed using siRNA. Primary human LSEC were transfected with either Accell human siGSK3b smart pool or a non-target control siRNA (NT) (Horizon Discovery/Dharmacon, Cambridge, UK) and cultured for 72 h, followed by treatment with either vehicle or 500μM PA. Knock-down efficacy was assessed by western blotting or qPCR for GSK3β.

Immunoblot analysis. Deidentified human liver tissues obtained by liver biopsy or surgical hepatic resection from patients with normal livers, isolated steatosis, or MASH were acquired (Institutional Review Board (IRB) #22-000320) and homogenized in T-PER lysis buffer (#78510, Roche) containing protease and phosphatase inhibitors (#78442, Thermo Scientific). Cells were lysed using RIPA buffer (50 mM Tris-HCl, pH 7.4; 1% Nonidet P-40; 0.25% sodium deoxycholate; 150 mM NaCl; 1 mM EDTA with protease inhibitors), followed by centrifugation at 15,000 × g for 15 min at 4°C. Protein concentrations in the lysates were measured using the Bradford assay (Sigma-Aldrich). Equal amounts of protein were loaded onto sodium dodecyl sulfate (SDS)-sulfate-polyacrylamide gel electrophoresis (PAGE) gels, transferred to nitrocellulose membranes (Bio-Rad, Hercules, CA, USA), and incubated overnight with the

primary antibody of interest. All primary antibodies were used at a dilution of 1:1,000 unless otherwise recommended by the manufacturer. Horseradish peroxidase-conjugated secondary antibodies against rabbit (Alpha Diagnostic International, San Antonio, TX, USA) or mouse (Southern Biotech, Birmingham, AL, USA) were used at a dilution of 1:5,000 and incubated for 1 h at room temperature. The proteins were detected using enhanced chemiluminescence reagents (GE Healthcare, Chicago, IL, USA). β-actin and GAPDH protein levels were used as loading controls.

Transendothelial Migration (TEM) Assay. As previously described[4, 5], we conducted a monocyte transendothelial assay using a hydrated collagen gel (PureCol Type I collagen solution, Advanced BioMatrix, 5005) culture system. Primary human LSEC (100 μl of 0.5×10^6 cells/ml) were labeled with Vybrant DiI solution (Molecular Probes, MP22885) and plated on hydrated collagen gel in each well of a 96-well plate to form a monolayer and then treated with vehicle or PA with or without the GSK3 inhibitor LY2090314 at a concentration of 20 μM for 16 h. The human monocytic cell line THP-1 (100 μl of 0.5×10^6 cells/ml) was labeled with Vybrant DiO solution (Molecular Probes, MP22885) and added to each well of a confluent human LSEC monolayer grown on top of the hydrated collagen gels. THP-1 cells were allowed to migrate for 1 h at 37°C and 5% CO_2. The monolayers were washed 3 times with warm DPBS/RPMI (200 μl per wash) to remove unattached monocytes. Monolayers were then fixed and imaged, and monocyte transmigration was quantified by confocal microscopy (Zeiss, LSM-780).

Migration assay. Bone marrow-derived monocytes were isolated from C57BL/6J mice (Jackson Laboratory). Briefly, bone marrow was extracted from dissected mouse tibia and femur, and monocytes were isolated using a Monocyte Isolation Kit (#130-100-629, Miltenyi Biotech) as described by the manufacturer. The cells were resuspended in RPMI-1640 medium without

phenol red (#11835030, Gibco) and fluorescently labeled with CellTracker Red CMTPX (#C34552, Invitrogen). Cells were treated for 30 min with vehicle (dimethyl sulfoxide), GSK3 inhibitors (LY 100 nM or ING 1 μM), or cenicriviroc (1 μM, #HY-14882A, MedChemExpress) in transwell inserts (5 μm pores, #3421, Corning) placed in a 24-well plate. RPMI medium with or without 100 ng/ml recombinant murine CCL2 (#250-10, PeproTech) was loaded into the bottom of the lower chamber of the 24-well plate. Cells were allowed to migrate for 3 h, after which the migrated cells in the lower chamber were counted using an automated plate-based imaging cytometer (Nexcelom Celigo S Imaging Cytometer).

Flow-based adhesion assay. Primary neutrophils were isolated from whole blood drawn from healthy adult volunteers (Institutional Review Board (IRB) #22-000320) using a human neutrophil isolation kit following the manufacturer's instructions (130-104-434, Miltenyi Biotec, Germany) and used within 4 h of isolation. Primary human LSEC were cultured in a collagen-coated Ibidi μ-Slide I Luer 0.4 (Cat #80176, Ibidi, Germany), and pre-treated with the GSK3 inhibitor LY2090314 (LY) 20 nM for two hours, then treated with PA 500 μM with or without LY overnight. A perfusion system with endothelial basal medium was connected and a shear flow of 0.8 dyne/cm^2 was applied. Freshly isolated neutrophils were incubated at 37°C for 30 min before being injected into the perfusion system. We then flushed 1.7 x 10^6 neutrophils per condition through the LSEC monolayer for 30 min, and non-adherent neutrophils were washed away by flushing the slide with basal medium for 20 min. Primary mouse LSEC were isolated as previously described [2]. A similar adhesion assay was performed to evaluate adhesion of primary mouse monocytes to primary mouse LSECs. Monocytes were isolated from healthy mice, and LSECs were isolated from either chow-fed vehicle-treated or CDHFD diet fed vehicle/9-ING-41 treated

mice as described previously. Bright-field images were taken, and adherent and transmigrated neutrophils or monocytes were counted using the Fiji software.

Animals. The study protocols were approved by the Institutional Animal Care and Use Committee (IACUC) of the Mayo Clinic. The methods employed in the current study were conducted according to the IACUC guidelines for the use of anesthetics in experimental mice. Mice were housed and bred in a temperature-controlled 12:12-hour light-dark cycle facility with free access to food. All interventions were performed during the light cycle. C57BL/6J mice were purchased from Jackson Laboratory (Bar Harbor, ME, USA).

Diet-induced Murine NASH Models. Eight-week-old C57BL/6J wild-type (WT) mice were fed either a chow diet (5053 PicoLab Rodent Diet 20; LabDiet, St. Louis, MO, USA) or a diet rich in fat, fructose, and cholesterol (FFC), starting at the age of 8-weeks for 24 weeks. The FFC diet consisted of 40% energy as fat (12% saturated fatty acid, 0.2% cholesterol) (AIN-76A Western Diet, TestDiet, St Louis, MO), with fructose (23.1 g/L), and glucose (18.9 g/L) in drinking water. The FFC diet-induced metabolic dysfunction associated with steatohepatitis (MASH) phenocopies the human disease and associated metabolic syndrome[6] and has been well validated by us[7, 8]. At 20 weeks on the diet, the mice were randomized to receive either vehicle or the GSK3 inhibitor LY2090314 intraperitoneally at 10 mg/kg body weight/dose 3 times a week for the last 4 weeks of the study. The dose employed was optimized based on a previously published study in a different disease model[9] and a pilot study in FFC-fed mice with dose modification to maintain tolerance. In an independent study, Eight-week-old C57BL/6J WT mice were fed a choline-deficient high-fat diet (CDHFD) (A06071302, Research Diet), which consists of 60% fat, 0.1% methionine, and no added choline, starting at 8 weeks of age for 6 weeks. Mice fed the CDHFD experienced minimal body weight loss as opposed to those fed the traditional methionine and choline-deficient

diet and had hepatic steatosis, ALT elevation, hepatocyte ballooning, hepatic inflammation, and fibrosis, recapitulating the histological features of human NASH, as shown in previous studies[1, 10]. Elraglusib (9-ING-41) was gifted by Acuate Therapeutics Inc. (Fort, Worth, TX), the dose employed was 30 mg/kg/day IP for 2 weeks during the last 2 weeks of the feeding study, was based on extensive pharmacodynamic and pharmacokinetic profiling by the company, and was the same dose employed in a different disease model[11].

Assessment of metabolic profiles in mice. At the 3rd week of LY treatment, total caloric intake was calculated based on the weight of food and drinking water consumption. Metabolic parameters, including oxygen consumption, carbon dioxide production, and respiratory exchange ratio, were measured using a comprehensive laboratory animal monitoring system (CLAMS; Columbus Instruments, OH, USA). These calorimetry chambers were also equipped with sensors that allowed the measurement of physical activity. Lean verus fat body composition was measured using echo-MRI. Blood glucose and plasma insulin levels were measured using Assure 4 (Arkray, Edina, MN) and Ultra-Sensitive Mouse Insulin enzyme-linked immunosorbent assay (ELISA) kits (Crystal Chem Inc., Downers Grove, IL), respectively. The homeostasis model assessment of insulin resistance (HOMA-IR) was calculated using the following formula: HOMA-IR = 26 × fasting insulin level (ng/mL) × fasting glucose level (mg/dL)/405[1].

Measurement of liver triglyceride and alanine aminotransferase levels. Liver triglyceride (TG) levels were measured in the mouse liver homogenates. Fifty milligrams of liver tissue were homogenized in a 5% NP-40 solution. The EnzyChrom Triglyceride Kit (BioAssay System, CA, USA) was used according to the manufacturer's instructions. The photometric absorbance was read at 570 nm using a Synergy H1 microplate reader (BioTek). Serum alanine aminotransferase

(ALT) levels were measured using VetScan2 (Abaxis Veterinary Diagnostics, Union City, CA, USA).

Histological, immunohistochemical, and digital imaging analyses. Hematoxylin and eosin (H&E) and Sirius red staining were performed as previously described[12]. Histology was assessed using the non-alcoholic fatty liver disease (NAFLD) activity score (NAS), a semi-quantitative score that accounts for steatosis, ballooned hepatocytes, and lobular inflammation[13]. Sirius red-stained tissue was imaged using red fluorescence and individual collagen fibers were automatically detected and quantified for width, length, and straightness using CT-FIRE [14, 15]. The tissue area was determined using ImageJ software. Formalin-fixed paraffin-embedded mouse liver tissue sections were deparaffinized, hydrated, and stained with antibodies against F4/80 (1:500), ICAM-1 (1:2,000), MPO (1:1,000), or α-SMA (1:1,000). The bound antibody was detected using a Vectastain ABC kit for goat (PK-6105 or PK-6101, Vector Laboratories, Burlingame, CA) and DAB substrate (Vector Laboratories) according to the manufacturer's instructions. Tissue sections were counterstained with hematoxylin. MPO staining was evaluated by immunofluorescence with an anti-goat alexa-568 secondary antibody (#A-11057, Thermo Fisher Scientific). Liver injury was assessed by the number of apoptotic hepatocytes using the terminal deoxynucleotidyl transferase deoxyuridine triphosphate nick-end labeling (TUNEL) assay and an In Situ Cell Death Detection Kit (Roche) following the manufacturer's instructions. The H&E-stained slides and ICAM1-stained slides were scanned using an Aperio AT2 scanner (Leica Biosystems) at 20X magnification at the pathology research core at the Mayo Clinic. The slides were annotated by a liver pathologist using Qupath 0.4 [14] for the central vein (CV) and portal vessel (PV) locations. The whole-slide images were then analyzed using a nonparametric supervised machine learning method through a Gaussian Process

(GP). A nonlinear boundary between different zones was acquired using nonlinear regression, showing the anatomical distance to the boundary annotations of both the CV and PV. A Gaussian process (GP) regression was used to predict the target value of-1 on the CV boundary contours and +1 on the PV boundary. A topographic map was constructed with three boundaries between zones determined by the level curve, with a GP output of -0.5 and +0.5. The whole slide images with the 3-zones contour were then analyzed using Qupath for ICAM-1 staining positivity surface area in each zone through an OpenCV pixel classifier using the diaminobenzidine (DAB) channel with a fixed threshold of 0.6 and a Gaussian prefilter at 1. The results included quantification of the ICAM-1 positive area within each zone. Steatosis quantification was performed using a machine learning algorithm trained on human liver biopsies [16].

Ultrasound-Based Liver Elastography. The mice were anesthetized with inhaled isoflurane (2-3%), shaved, and depilated. The mice were placed in the supine position on an imaging platform with the temperature maintained at 37 °C. We employed high-frequency (22 MHz) ultrasound using a Vega system (SonoVol) to image the mice. The transducer was moved to the liver and the region of interest (ROI) was adjusted to include only liver tissue. Six consecutive 2D shear wave elastography (SWE) scans were taken at 0.5 mm intervals through the liver. The median Young's Modulus for the ROI for each scan was calculated using SonoEQ software (SonoVol) and then averaged for each animal. One-way ANOVA was used for statistical analysis of significance.

Tandem Mass Tag (TMT)-based on quantitative total and phospho-proteomics. As previously described, LSEC isolated from FFC-fed NASH or chow-fed control mice were subjected to liquid chromatography-mass spectrometry (LC-MS) sample preparation. [17] One hundred micrograms of protein from each sample was TCA-precipitated. After washing with acetone and methanol, the protein pellet was reconstituted in 100 µl of 200 mM HEPES (pH 8.5). The samples were digested

with Lys-C overnight at room temperature and then trypsinized for 6 h at 37°C at a 1:100 protease-to-protein ratio. To each digest 234, µg of TMTpro16plex reagents (12 µl) and 30 µl of 100% anhydrous acetonitrile were added for labeling (labels used: 126:293T Vehicle (V); 127N: 293T Torin1 (T); 127C: RPE1 V; 128N: RPE1 T; 128C: U2OS V; 129N: U2OS T; 129C: HeLa V; 130N: HeLa T; 130C: MCF7 V; 131N: MCF7 T; 131C: HCT116 V; 132N: HCT116 T; 132C: Panc1 V; 133N: Panc1 T; 133C: RKO V; 134N: RKO T). The samples were then labeled for 60 min at room temperature. Two microliters (1.4% v/v) of each sample was pooled, desalted, and analyzed by MS to check the labeling efficiency. After checking the labeling efficiency, the samples were quenched by adding 5 µl of 5% hydroxylamine and pooled. The pooled samples were desalted using 200 mg Sep-Pak solid-phase extraction columns. A Pierce High-Select Fe-NTA phosphopeptide enrichment kit was used to enrich phosphopeptides from the pooled mixture. The unbound fraction and column washes were combined, desalted, and fractionated by bRPLC. Fractions were collected in a 96-well plate and combined for a total of 24 fractions (A and B sets) before desalting and subsequent LC–MS/MS analysis.

Integrated omics analysis. Differentially expressed genes (p-value < 0.05) between chow-fed mice and FFC-fed mice in the LSEC total proteomic analysis or our previous LSEC transcriptomic analysis (GSE164006)[1]) were subjected to Kyoto Encyclopedia of Genes and Genomes (KEGG) overrepresentation pathway analysis. The mass spectrometry proteomics data were deposited in the ProteomeXchange Consortium via the PRIDE [18] partner repository with the dataset identifier PXD048073.

Nanostring-based gene expression profiling. The gene expression profile of HHSECs was assessed using a NanoString nCounter system (NanoString Technologies, Seattle, WA, USA). We employed the Human Fibrosis V2 panel, in which 760 fibrosis-related human genes and 10

housekeeping reference genes were implemented. All procedures, including sample preparation (100 ng of RNA per sample), hybridization (at 65°C for 17 h), detection, and subsequent analysis, were performed according to the manufacturer's instructions. After quality control and background thresholding using built-in negative control probes, the data were normalized to the positive hybridization controls and housekeeping genes.

Quantitative reverse transcription PCR (qRT-PCR). Total RNA was isolated using the RNeasy Mini Kit (Qiagen, Valencia, CA, USA) and reverse-transcribed with Moloney murine leukemia virus reverse transcriptase and oligo-dT random primers (both from Invitrogen, CA, USA). Gene expression was quantified by real-time PCR using SYBR green fluorescence on a LightCycler 480 instrument (Roche Applied, IN, USA) **(primers are listed in Supplementary Table 4)**. The target gene expression was calculated and normalized using the ΔΔCt method.

Mass Cytometry by time-of-flight (CyTOF) analysis. Four random mice from each cohort were selected for intrahepatic leukocyte isolation by using a liver dissociation kit and Percoll gradient centrifugation. Cells were suspended in Maxpar Cell Staining Buffer (CSB) (Fluidigm, San Francisco, CA) and labeled with 0.5 μM cisplatin (Fluidigm) solution. After centrifugation, the cells were resuspended in CSB before addition of the cell surface antibody staining cocktail in an equal volume of CSB. Cells were incubated with gentle agitation at room temperature for 45 min. Following a wash with CSB, samples were permeabilized with eBioscience FoxP3/Transcription factor/fixation/permeabilization solution (Thermo Fisher, Waltham, MA), washed, and resuspended in permeabilization buffer before the addition of the intracellular antibody staining cocktail. Cells were incubated at room temperature for 45 min with gentle agitation. Following washing with PBS, the cells were fixed with 2% paraformaldehyde using gentle agitation at 4°C for 30 min. Cells were washed with CSB and DNA intercalation was performed by adding 1:10000

diluted 125 μM of Cell ID™ Intercalator-Ir (Fluidigm) with gentle agitation at 4°C overnight. Cells were resuspended in a 1:10 dilution of EQ beads (EQ Four Element Calibration Beads, Fluidigm) and then loaded onto the Helios sample loader for data acquisition. Mass cytometry was performed in the Immune Monitoring Core at the Mayo Clinic, and antibodies conjugated to stable heavy metal isotopes were employed to detect cellular antigens by mass cytometry time-of-flight (CyTOF) and enable comprehensive profiling of the phenotype and function of intrahepatic leukocytes. After data acquisition, fcs files were normalized using CyTOF Software (version 6.7.1014). Cleanup of cell debris, removal of doublets, and dead cells were performed using FlowJo software version 10.5.3 (Ashland, OR). The cleaned fcs files were analyzed using the R-based tool CyTOF kit version 3.8[19]. Clustering and dimensionality reduction to 20,000 events per file were performed using the Rphenograph algorithm, which included 32 different cell surface markers and two cytosolic markers (S100A8 and MPO) in the panel **(Supplementary Table 1-3, Fig. S8)**. Visualization of the clusters was performed using a tSNE map. Relative marker intensities and cluster abundances per sample were visualized using a heat map.

Statistical analysis. Data are expressed as mean ± SEM. Differences between multiple groups were compared using one-way analysis of variance followed by Bonferroni's multiple comparisons test or Student's t-test when comparing two groups. *, **, ***, **** indicate statistical significance with $p < 0.05$, $p < 0.01$, $p < 0.001$ and $p < 0.0001$, respectively. Statistically non-significant results are labeled as ns, where appropriate. All analyses were performed using the GraphPad Prism 9.2.0 software (CA, USA).

Supplementary figures

Fig. S1

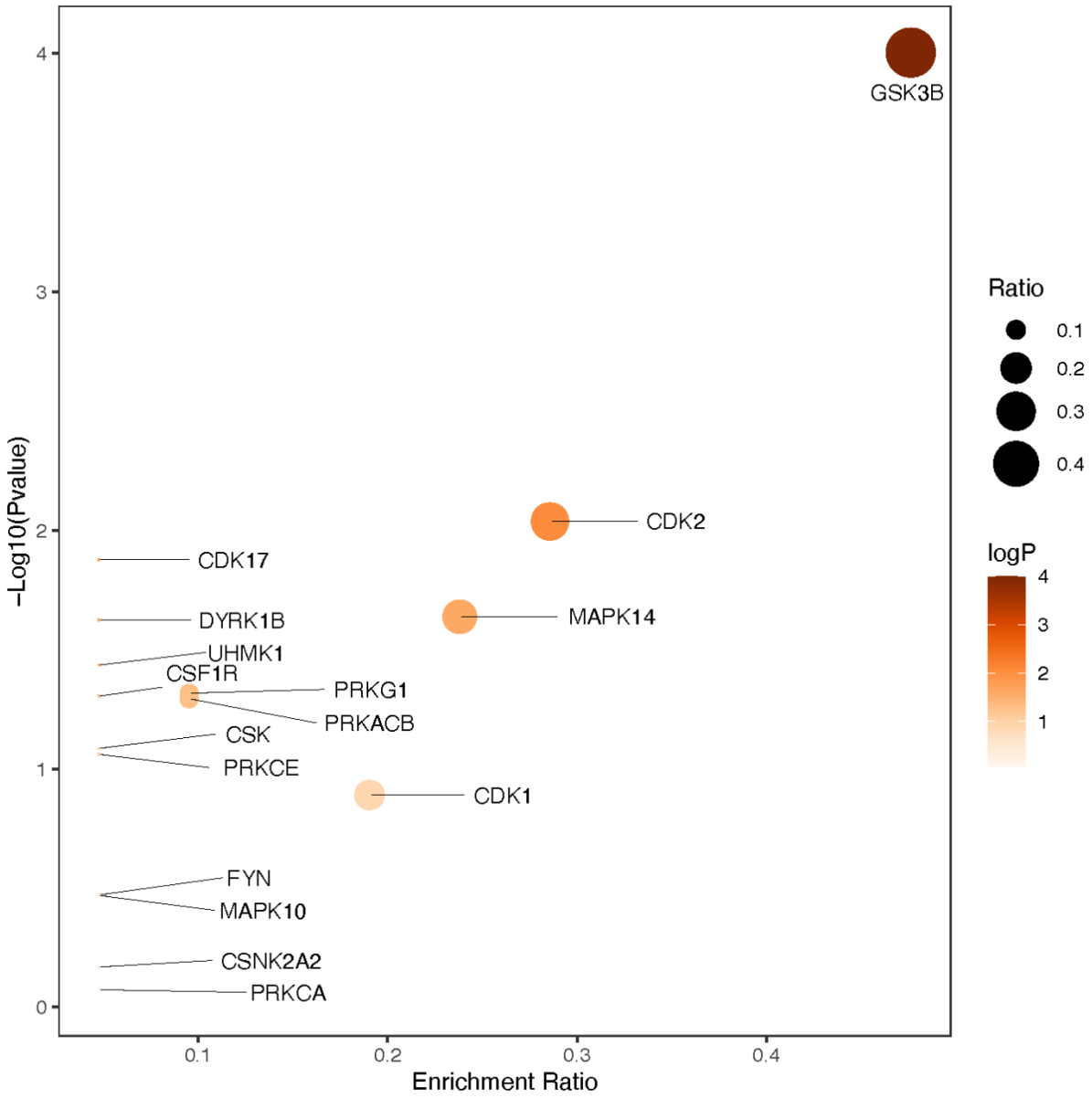

Fig. S1. GSK3β is the top hub kinase altered in the MASH LSEC. Enrichment ratio (bubble size) and log (p-value) values for the top 16 ranked putative altered kinases in FFC versus chow-fed mice generated from the phospho-proteomic study are shown in **(Figure 1A).**

Supplemental Figure 2

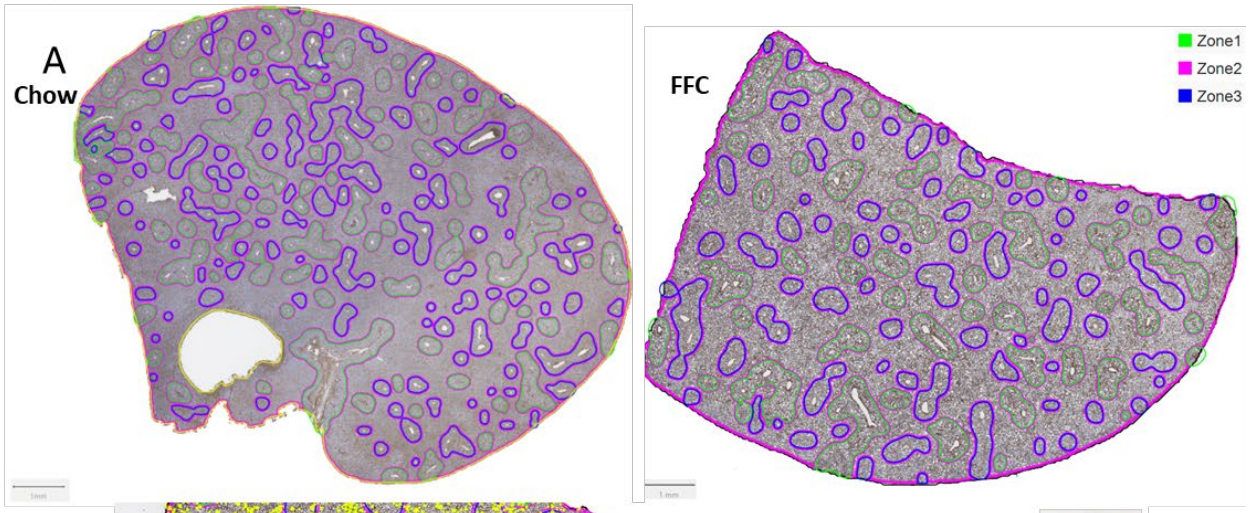

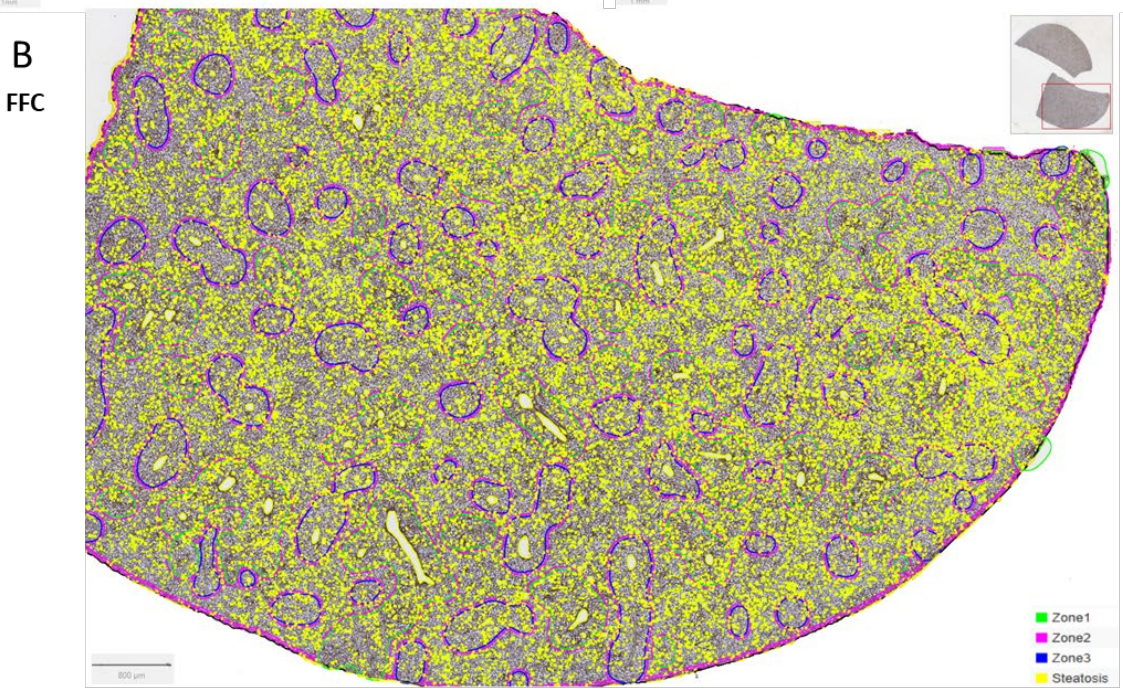

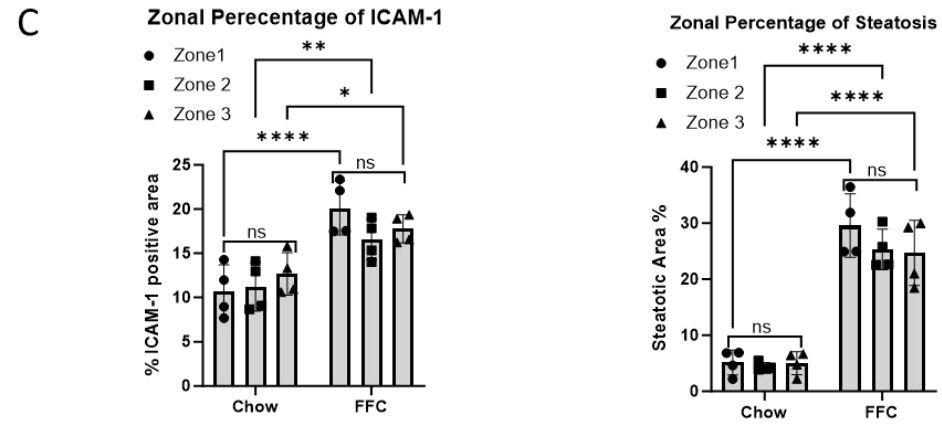

Fig. S2. Zonal distribution of lipotoxic endotheliopathy in vivo. *(*A) Images of digitized whole slides from mice with FFC diet-induced MASH and chow control; the slides were immunostained for ICAM-1, and zonal annotations were performed by the liver pathologist. (B) Image of a digitized whole slide from a mouse with FFC diet-induced MASH immunostained for ICAM-1 with zonal annotation and zonal steatosis representation using a machine learning algorithm. (C) Zonal percentages of ICAM-1 positive areas and-steatotic areas**.** (n=4 per group); bar graphs represent the mean ± SEM, *$p < 0.05$, **$p<0.01$, ****$p< 0.0001$, ns, non-significant (One-way ANOVA with Bonferroni's multiple comparison).

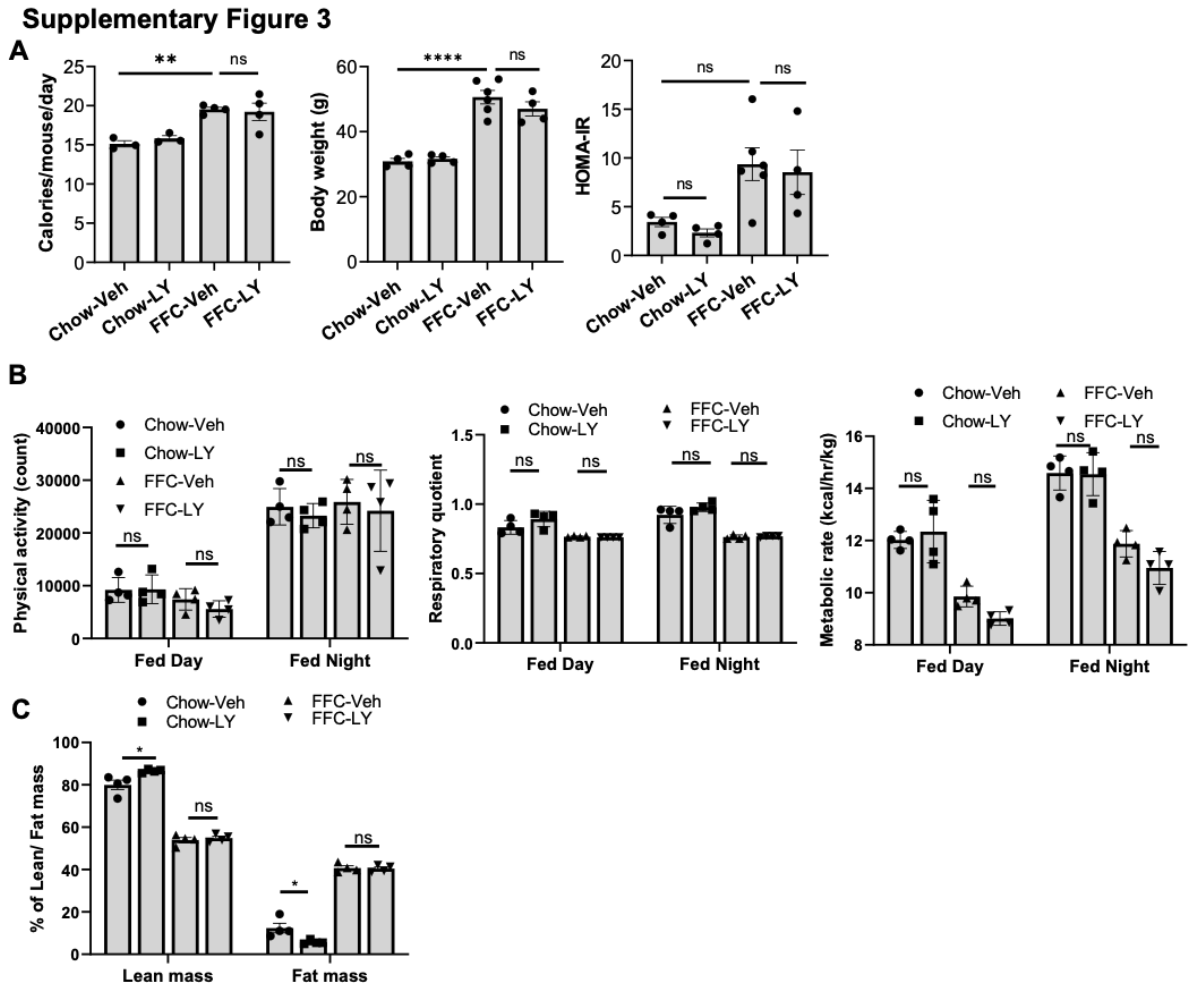

Fig. S3. LY2090314 was well-tolerated and did not affect insulin resistance or metabolic phenotypes in diet-induced murine MASH. Eight-week-old wild-type C57BL/6J mice were fed either a chow or FFC diet for 24 weeks to induce MASH and treated with either vehicle (Veh) or the GSK3 inhibitor LY2090314 (LY) for the last 4 weeks. (A) Daily caloric intake (left), body weight (middle), and HOMA-IR (right). (B) Physical activity, normalized respiratory quotient, and metabolic rate were assessed using the CLAMS study, and (C) lean versus fat mass body composition measured using Echo-MRI. Bar graphs represent mean ± SEM, *p < 0.05, **p<0.01, ****p< 0.0001, ns, nonsignificant (One-way ANOVA with Bonferroni's multiple comparison)

Supplementary Figure 4

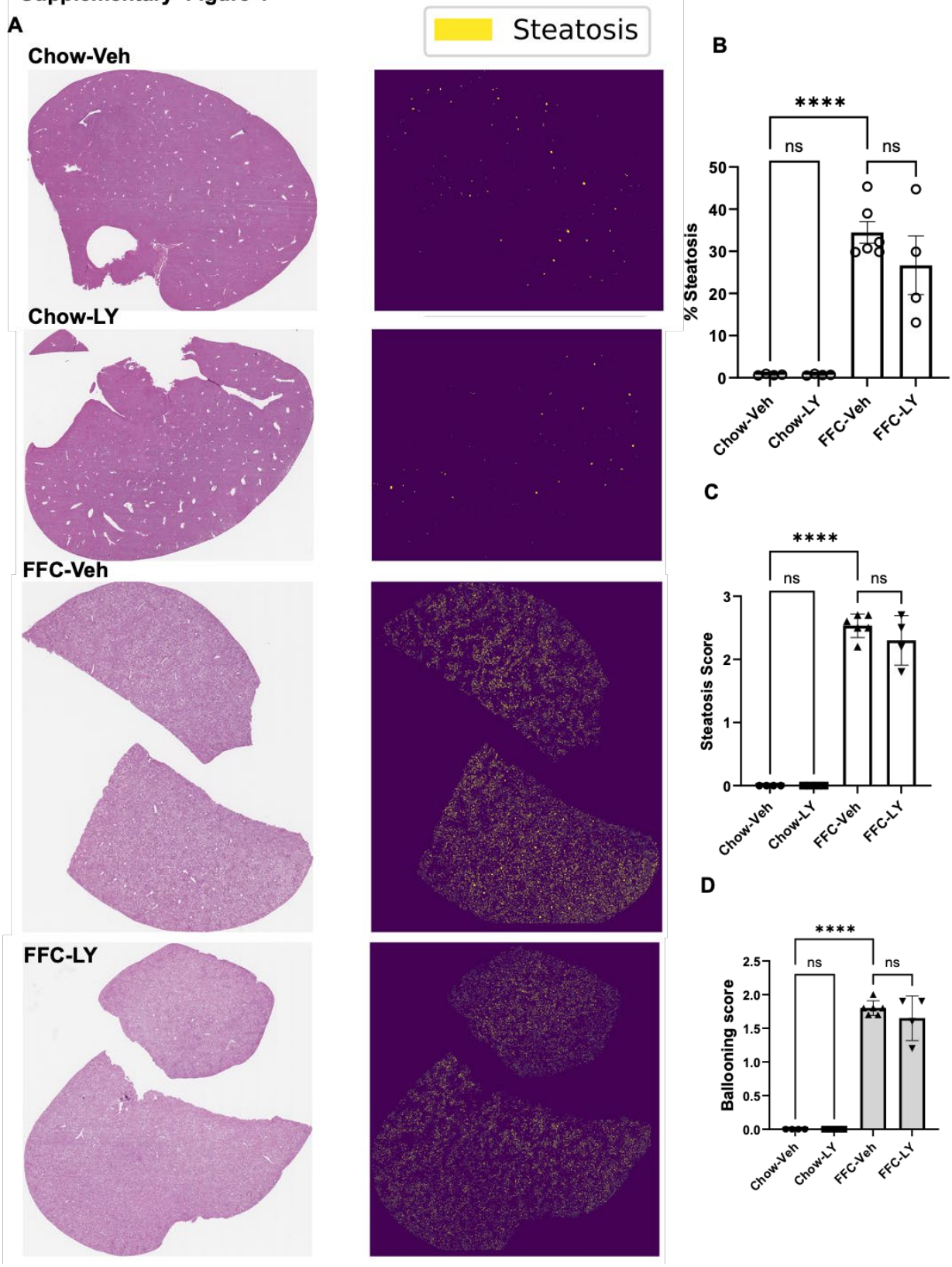

Fig. S4. LY treatment did not significantly reduce steatosis in MASH-treated mice. (A) Representative images of whole digitized H&E-stained slides and the corresponding steatotic areas from Chow- and FFC-fed mice treated with either vehicle or LY. (B) Automated quantification of steatosis percentage on digitized H&E-stained slides. (C) Steatosis scoring performed by estimating the steatotic area percentage in five fields per mouse and averaging (score 1 (6-33%), score 2 (33-66%), score 3 more than 66%)]. (D) Ballooning scores. (n=4-6 per group); bar graphs represent mean ± SEM, ****$p < 0.0001$, ns, non-significant (One-way ANOVA with Bonferroni's multiple comparison).

Supplementary Figure 5

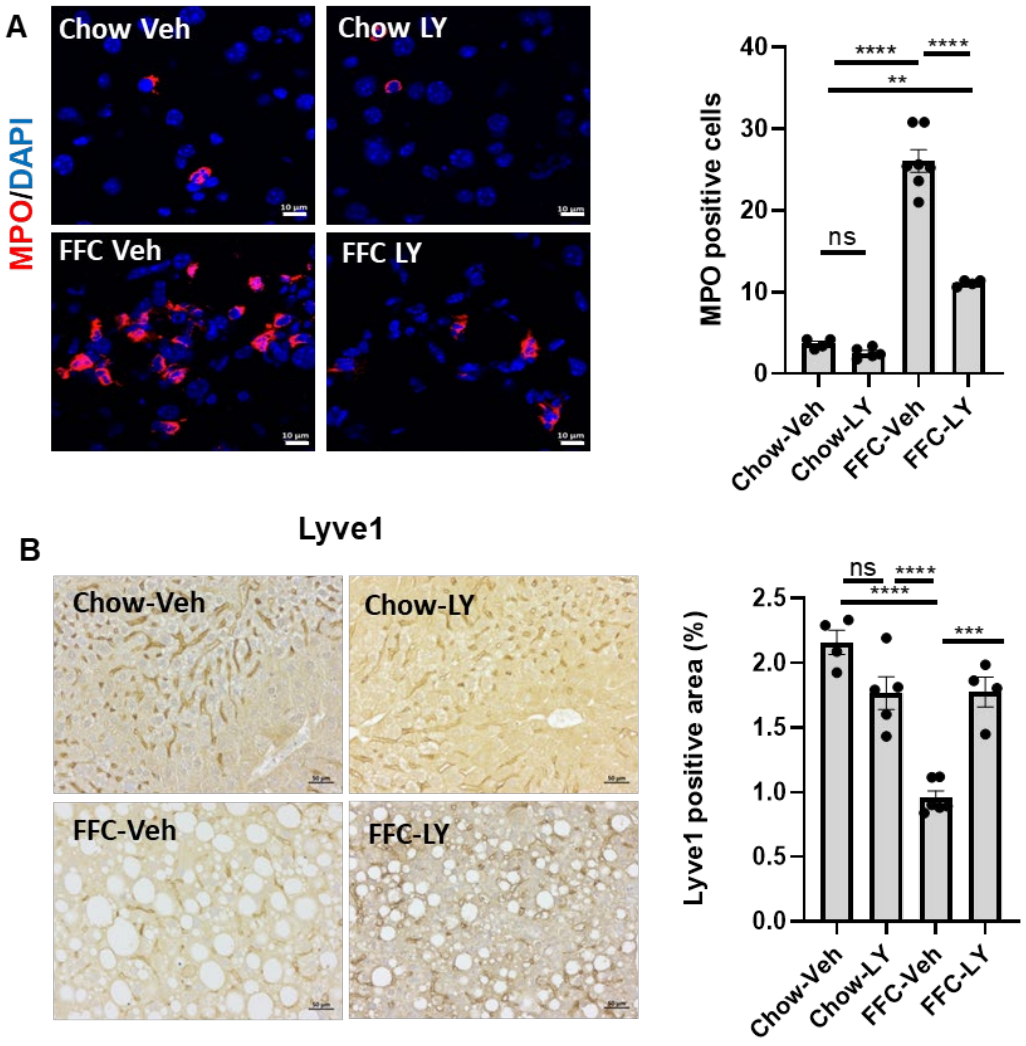

Fig. S5. LY treatment reduces hepatic neutrophil infiltration and restores LSEC differentiation in murine MASH. Representative images (A) for MPO immunofluorescence staining (red) and nuclei were stained with DAPI (blue). Images are shown at a 63x magnification. Scale bar: 10 µm. (B) Lyve 1 immunostaining of the liver sections (left). MPO and Lyve1 positive areas were quantified in 5 random 10x microscopic fields and averaged for each animal (right panel). Scale bar: 50 µm (n=4-6 per group) Bar graphs represent mean ± SEM, **p< 0.0001, ****p< 0.0001, ns, nonsignificant (One-way ANOVA with Bonferroni's multiple comparison).

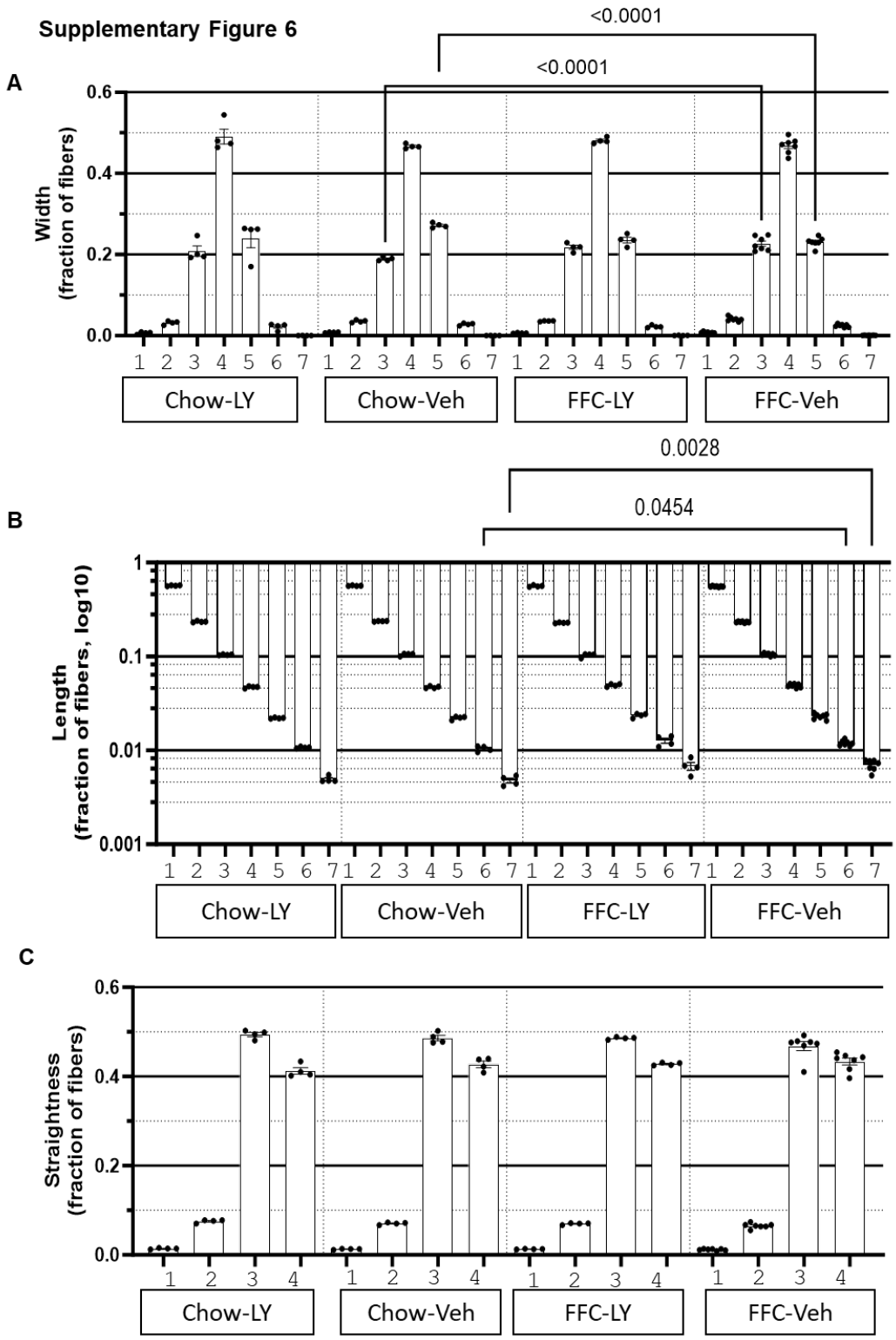

Fig. S6. Impact of the FFC diet on the fraction of hepatic collagen fiber width, length, and straightness. (A) Frequency histogram of collagen fiber width. The fiber widths were divided into

seven bins, from low (1) to high (7). Compared to regular chow, FFC increased the fraction of fibers in bin 3 and decreased the fraction in bin 5, indicating that FFC increased the prevalence of narrower fibers. Data are presented as mean ± SEM, n=4-7, p values by ANOVA. (B) Frequency histogram of the collagen fiber length. Fiber lengths were divided into seven bins from low (1) to high (7). FFC increased the fraction of longer fibers (bins 6 and 7). Data are presented as mean ± SEM, n=4-7, p values by ANOVA. (C) Frequency histogram of collagen fiber straightness. Fiber straightness was divided into four bins from low (1) to high (4). Neither FFC nor LY affected the distribution of fibers vs chow or FFC-Veh controls, respectively. Data are presented as mean ± SEM, n=4-7, p values by ANOVA.

Supplementary Figure 7

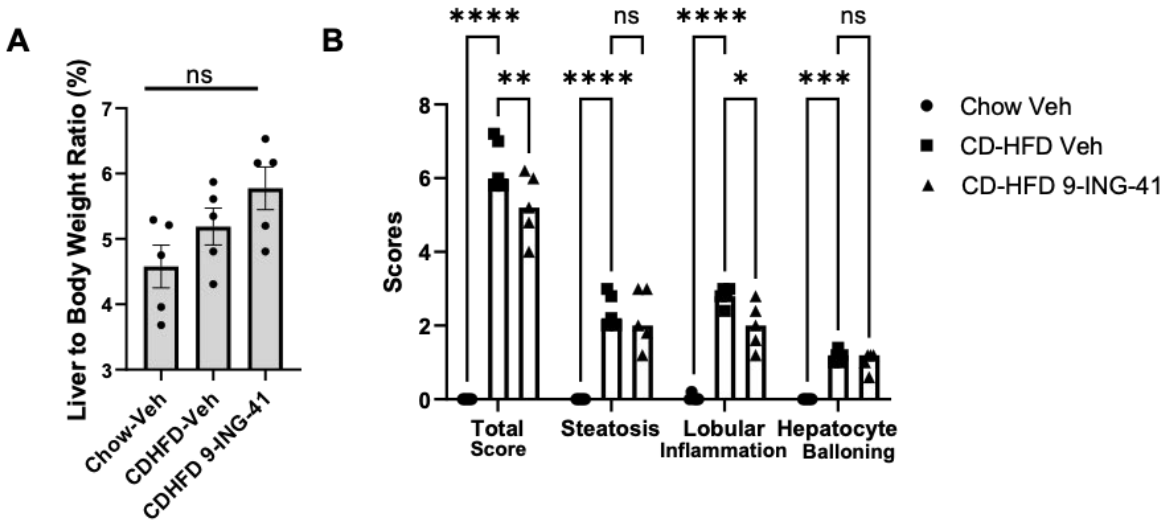

C

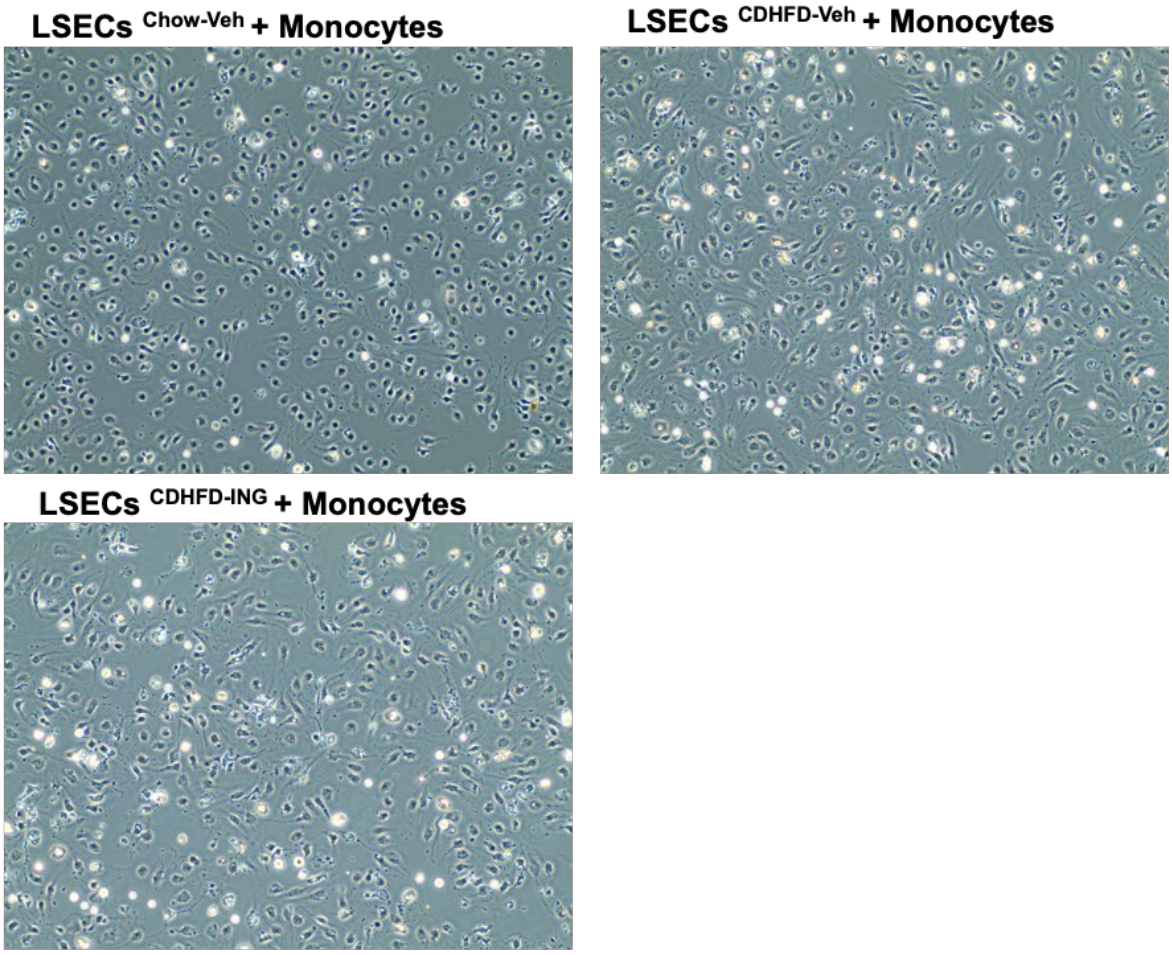

Fig. S7. 9-ING-41 treatment in MASH mice reduced lobular inflammation and monocyte adhesion to LSEC. Mice were fed chow or a CDHFD and treated with either vehicle or 9-ING-41 (A)**.** The liver-to-body weight ratio was also measured. (B) Steatosis, lobular inflammation, and hepatocyte ballooning were assessed using the NASH Clinical Research Network Scoring System (NAS). (C) Representative images of adherent bone marrow-derived monocytes to LSEC from control mice versus mice with diet-induced MASH treated with either vehicle or 9-ING-41 (n=5); bar graphs represent mean ± SEM, *p < 0.05, **p<0.01, ***p< 0.001, ****p< 0.0001, ns, non-significant (One-way ANOVA with Bonferroni's multiple comparison).

Supplementary Figure 8

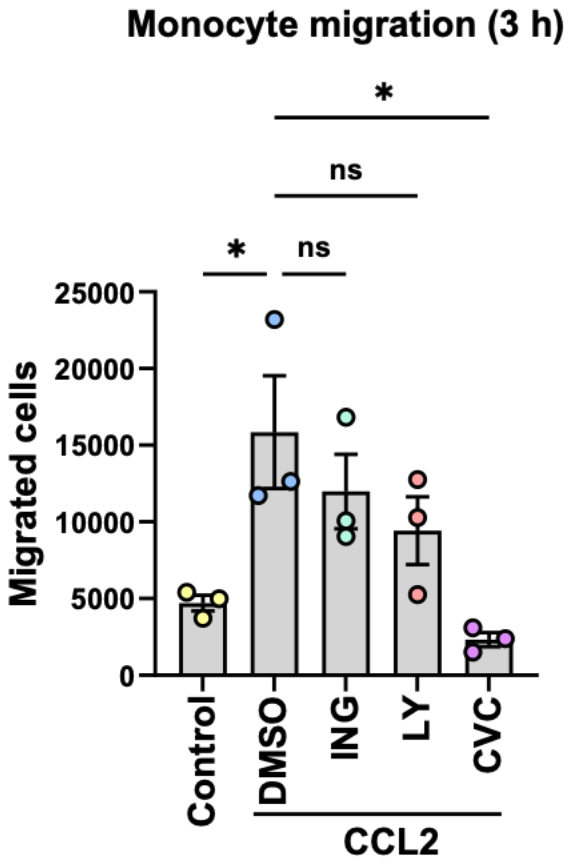

Fig. S8. Monocyte migration was not significantly altered by GSK3 inhibition, and monocytes were isolated from chow-fed mice and treated with the chemokine CCL2 (100 ng/ml) ± GSK3 inhibitors (LY 100 nM or ING 1 μM) or cenicriviroc (1 μM) in transwell inserts placed in a 24-well plate and allowed to migrate for 3 h. Migrated cells in the lower chamber were counted using an automated plate-based imaging cytometer (n=3 per group); bar graphs represent mean ± SEM, *$p < 0.05$, ns, non-significant (One-way ANOVA with Bonferroni's multiple comparison).

Supplementary Figure 9

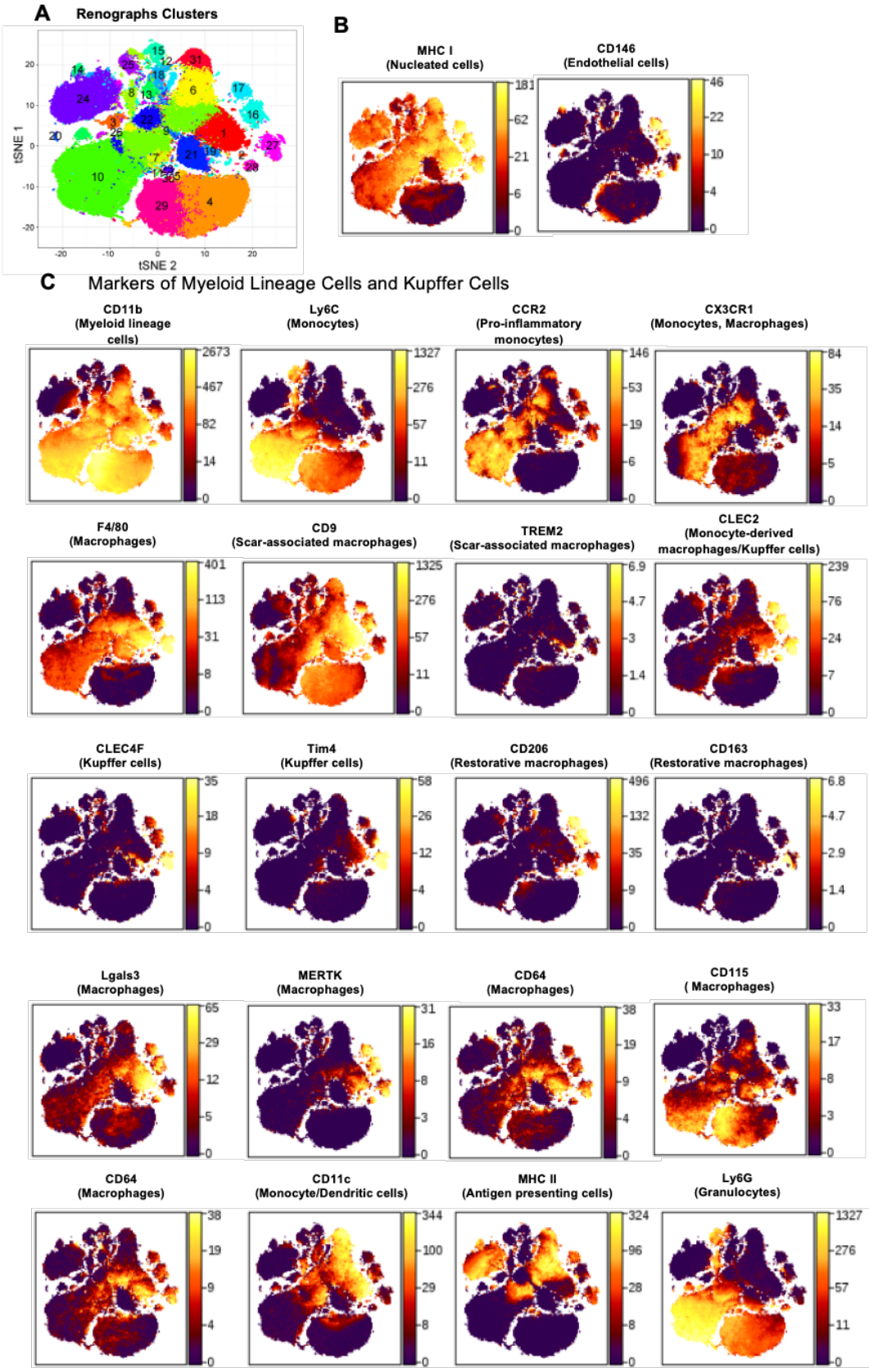

Supplementary Figure 9 (continued)

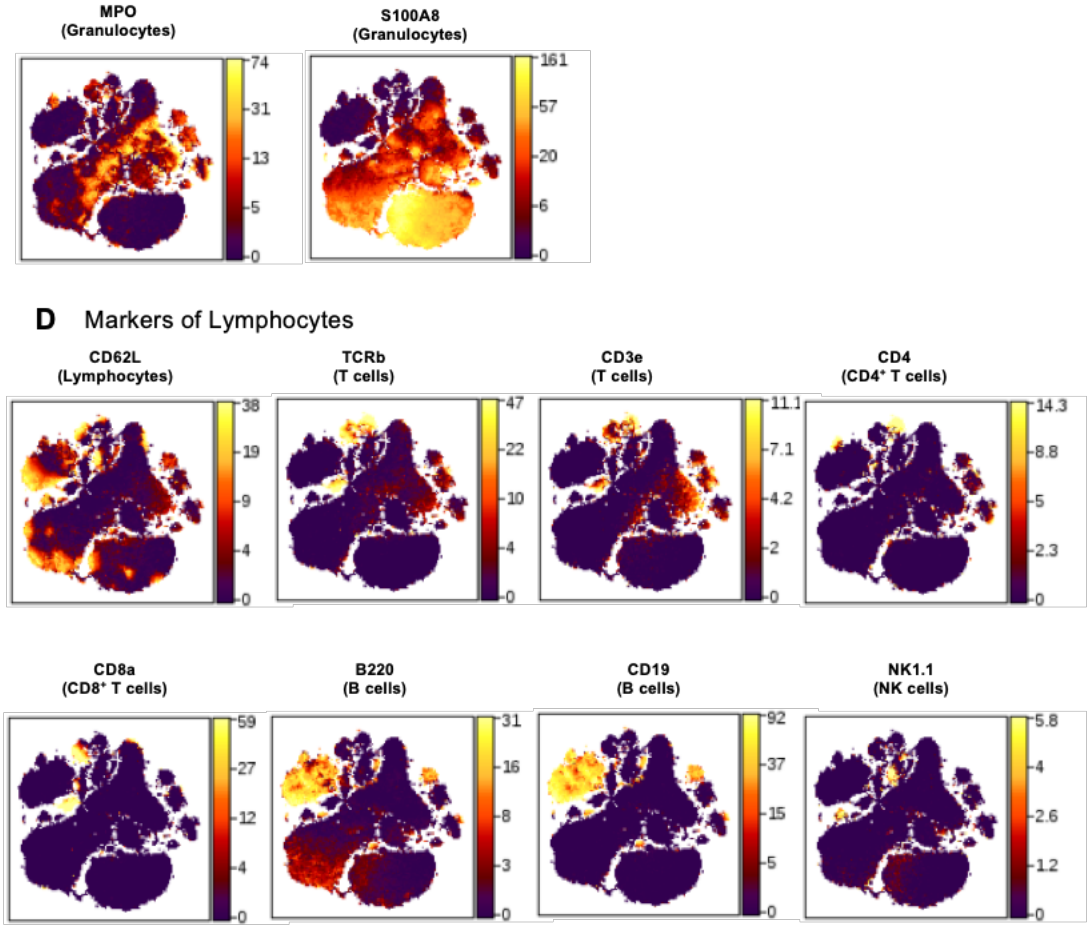

Fig. S9. Intrahepatic leukocyte (IHL) profiling by mass cytometry by time-of-flight (CyTOF). CyTOF was performed on IHL of control vehicle-treated chow-fed mice, and CDHFD-fed mice treated with either 9-ING-41 or vehicle. Thrirty-one unique clusters were defined using a panel of 32 different cell surface markers and two cytosolic markers (shown in Supplementary Table 1-2). (A) t-distributed stochastic neighbor embedding (tSNE) plot generated using the Rphenograph clustering algorithm (identical to Figure 7A). (B) tSNE plots depicting the density of MHC-I, and CD146 positive cells in each cluster. (C and D) tSNE plots depicting cell surface marker densities for (C) myeloid-lineage cells and Kupffer cells and (D) lymphocytes in each cluster.

Supplementary Figure 10

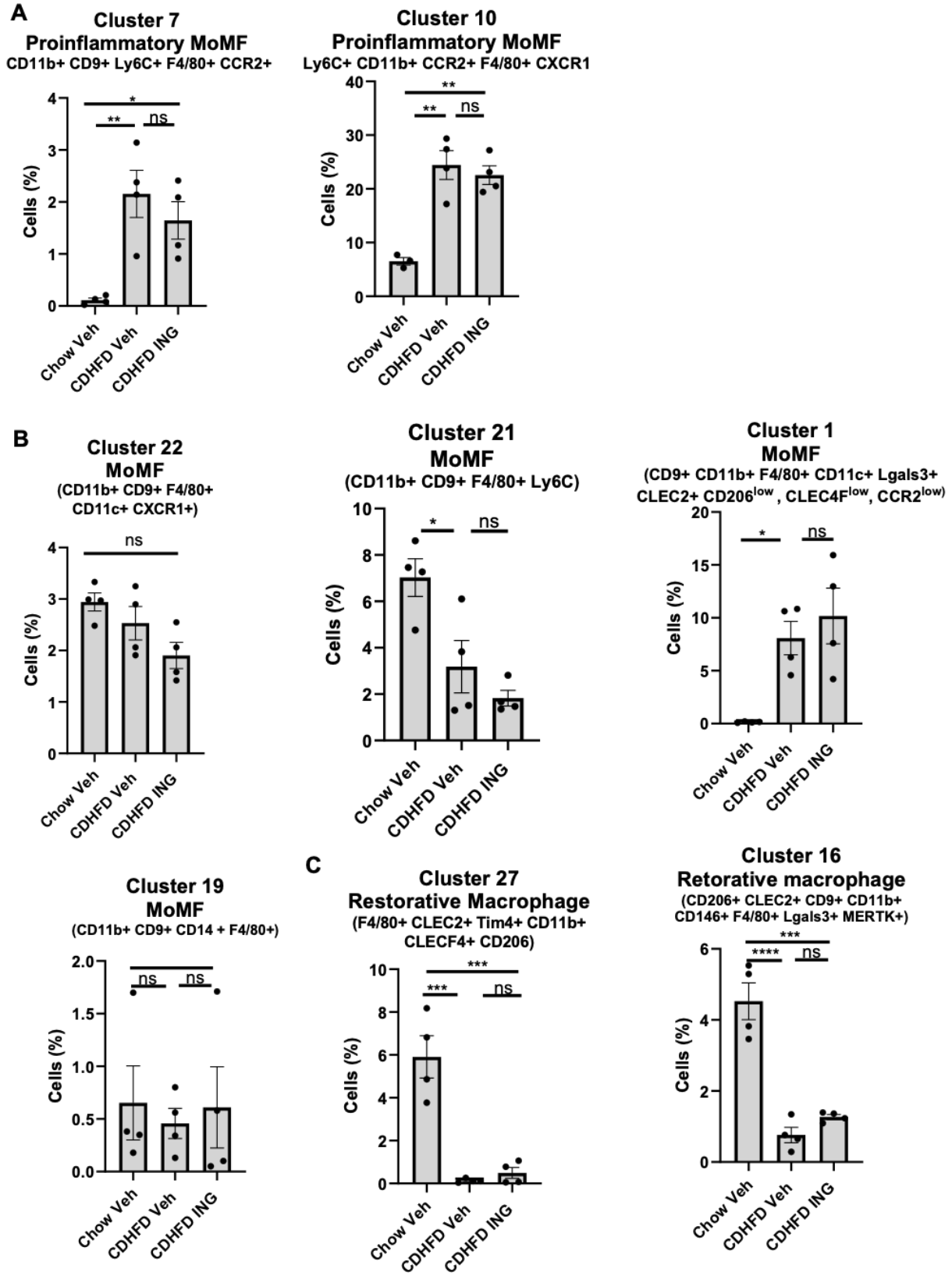

Supplementary Figure 10 (Continued)

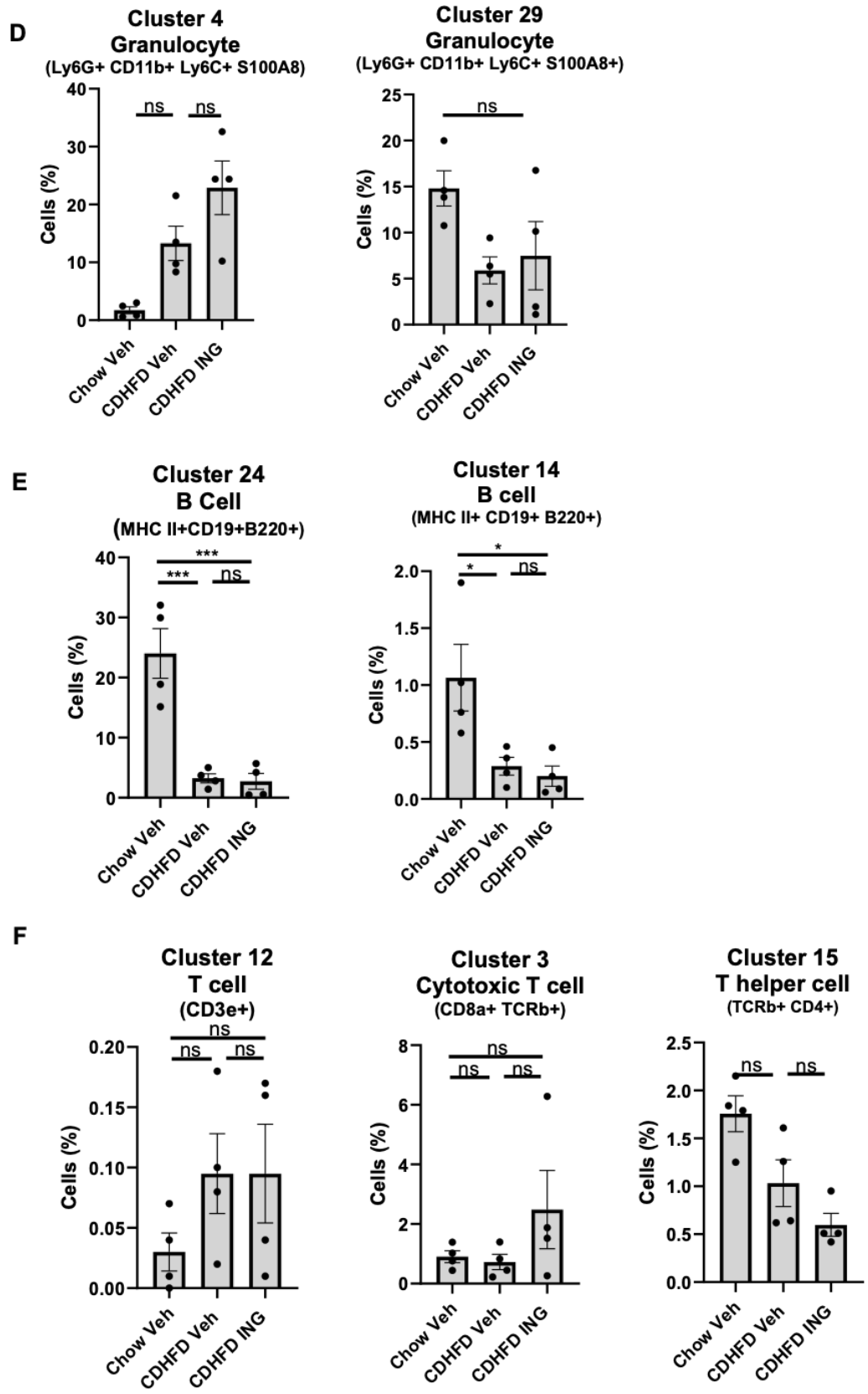

Fig. S10. 9-ING-41 treatment of CDHFD-fed mice does not significantly alter the granulocyte, T cell, or B cell populations. The proportion of cells in specific clusters was quantified for each experimental group. (A) Clusters 7 and 10 were categorized into proinflammatory monocyte-derived macrophages (MoMF), (B) Clusters 22, 21, 1 and 19 into monocyte-derived macrophages (MoMF), (C) Clusters 27 and 16 into restorative MoMF, (D) Clusters 4 and 29 into granulocytes, and (E) Clusters 24 and 14 into B cells, (F) Cluster 12 into T cells, Cluster 3 into cytotoxic T cells, Cluster 15 into T helper cell (n=4 per group); bar graphs represent mean ± SEM, *$p < 0.05$, **$p<0.01$,***$p<0.001$,****$p<0.0001$ ns, nonsignificant (One-way ANOVA with Bonferroni's multiple comparison).

Supplementary tables

Table S1

No.	Sp.	Label	Target	Clone	Company	Catalog Number
1	Ms	089Y	CD45	30-F11	Fluidigm	3089005B
2	Ms	106Cd	CD146	ME-9F1	Biolegend	134702
3	Ms	112Cd	CD4	RM4-5	Biolegend	100561
4	Ms	116Cd	MPO	EPR20257	Abcam	ab221847
5	Ms	141Pr	Lgals3	202213	R&D Systems	MAB1197
6	Ms	142Nd	CD11c	N418	Fluidigm	3142003B
7	Ms	143Nd	TCRb	H57-597	Fluidigm	3143010B
8	Ms	144Nd	MHC Class I	28-14-8	Fluidigm	3144016B
9	Ms	145Nd	CLEC-2 (CLEC1B)	17D9/CLEC-2	Biolegend	146102
10	Ms	147Sm	CD9	MZ3	Biolegend	124802
11	Ms	148Nd	CXCR2	SA044G4	Biolegend	149302
12	Ms	149Sm	Tim4	RMT4-54	BioLegend	130002
13	Ms	151Eu	CD206 (MMR)	C068C2	BioLegend	141702
14	Ms	152Sm	CD3e	145-2C11	Fluidigm	3152004B
15	Ms	153Eu	CLEC4F/CLECSF13	poly Goat	R&D	AF2784
16	Ms	154Sm	CD62L (L-selectin)	MEL-14	BioLegend	
17	Ms	155Gd	MERTK	108928	R&D Systems	MAB5912
18	Ms	156Gd	CCR2	475301	R&D Systems	MAB55381
19	Ms	159Tb	F4/80	BM8	Fluidigm	3159009B
20	Ms	160Gd	CD64	290322	R&D Systems	MAB20741
21	Ms	161Dy	Ly6G	1A8	BioLegend	127637
22	Ms	164Dy	CX3CR1	SA011F11	Fluidigm	3164023B
23	Ms	165Ho	CD14	Sa14-2	BioLegend	123321
24	Ms	166Er	CD19	6D5	Fluidigm	3166015B
25	Ms	167Er	TREM2	237920	R&D	MAB17291
26	Ms	168Er	CD8a	53-6.7	Fluidigm	3168003B
27	Ms	169Tm	CD163	S15049	Biolegend	155302
28	Ms	170Er	CD161 (NK1.1)	PK136	Fluidigm	3170002B
29	Ms	172Yb	CD11b (Mac-1)	M1/70	Fluidigm	3172012B
30	Ms	173Yb	S100A8	63N13G5	NOVUS	NBP2-25273
31	Ms	174Yb	CD115/CSF1R	AFS98	BioLegend	135521
32	Ms	175Lu	Ly6C	HK1.4	BioLegend	128039
33	Ms	176Yb	CD45R (B220)	RA3-6B2	Fluidigm	3176002B
34	Ms	209Bi	I-A/I-E (MHC II)	M5/114.15.2	BioLegend	107637

Table S2

Antibody panel of 33 markers

Macrophages F4/80, CD64, Tim4, MERTK, CD206, CD163, Lgals3, CD115, CD14, CLEC2, CLEC4F, TREM2, MHCI	**Pan-leukocyte** CD45	**Dendritic cells** CD11c, MHCII
	Monocytes Ly6C, CCR2, CX3CR1, CD11b, CD14	**NK cells** NK1.1
		B cells B220, CD19
Neutrophils CD11b, Ly6G, **MPO, S100A8**	**T cells** CD3e, CD8a, TCRb, CD4	**LSEC** CD146

Table S3

Annotated Clusters Based on Surface Markers

Cluster number	Positive Surface Markers	Annotation
1	CD9+, CD11b+, F4/80+, CD11c+, Lgal3+, CXCR2+, CLEC2+ ,$CD206^{low}$, $CLEC4F^{low}$, $CCR2^{low}$	Monocyte derived Macrophage (MoMF) (CD11b+ F4/80+)
3	CD8a+, TCRb+	Cytotoxic T cells (CD8a+, TCRb+)
4	Ly6G+, CD11b+, Ly6C+	Granulocyte (Ly6G+)
6	CD11b+, CD11c+, MHCII+, CCR2+	Monocyte derived Dendritic cells (MoDC) (CD11b+ MHC II+ CD11c+)
7	CD11b+, CD9+, Ly6C+, F4/80+, CD11c+, CCR2+, CX3CR1+	Proinflammatory MoMF (CD11b+, F4/80+,CCR2+)
9	CD11b+, CD9+, F4/80+, CCR2+, CX3CR1+	Proinflammatory MoMF (CD11b+, F4/80+,CCR2+)
10	Ly6c+, CD11b+, CCR2+, CX3CR1+	Proinflammatory MoMF (CD11b+, F4/80+,CCR2+)
12	CD3e+	T cell (CD3e+)
14	MHCII+, CD19+, B220+	B cells (CD19+, B220+)
15	CD4+, TCRb+	T helper (CD4+, TCRb+)
19	CD11b+ CD9+ CD14 + F4/80+	MoMF (CD11b+ F4/80+)
21	CD11b+ CD9+ F4/80+ Ly6C	MoMF (CD11b+ F4/80+)
22	CD11b+ CD9+ F4/80+ CD11c+ CXCR1+	MoMF (CD11b+ F4/80+)
24	MHCII+, CD19+, B220+, CDL62+	B cells (CD19+, B220+)
29	Ly6G+, CD11b+, Ly6C+	Granulocyte (Ly6G+)
27	F4/80+ CLEC2+ Tim4+ CD11b+ CLECF4+ CD206+	Restorative Macrophage (F4/80+ CLECF4+ CD206+)
31	CD11b+, MHCII+, CD11c+, CCR2+	MoDC (CD11b+ MHC II+ CD11c+)

Table S4

PCR primers:

Name	**Sequence**
Mouse *Ccr2* Forward Primer	ATCCACGGCATACTATCAACATC
Mouse *Ccr2* Reverse Primer	CAAGGCTCACCATCATCGTAG
18S Forward Primer	CGCTTCCTTACCTGGTTGAT
18S Reverse Primer	GAGCGACCAAAGGAACCATA
Mouse *Col1a1* Forward Primer	GCTCCTCTTAGGGGCCACT
Mouse *Col1a1* Reverse Primer	CCACGTCTCACCATTGGGG
Human *CXCL2* Forward Primer	CATCGAAAAGATGCTGAAAAATG
Human *CXCL2* Reverse Primer	TTCAGGAACAGCCACCAATA
Mouse *Cxcl2* Forward Primer	CCAACCACCAGGCTACAGG
Mouse *Cxcl2* Reverse Primer	GCGTCACACTCAAGCTCTG
Human *ICAM-1* Forward Primer	TATAAAGGATCACGCGCCCC
Human *ICAM-1* Reverse Primer	GACTCACCTGGGAACAGAGC
Human *GSK3b* Forward Primer	GGCAGCATGAAAGTTAGCAGA
Human *GSK3b* Reverse Primer	GGCGACCAGTTCTCCTGAATC
Mouse *Col1α1* Forward Primer	GCTCCTCTTAGGGGCCACT
Mouse *Col1α1* Reverse Primer	CCACGTCTCACCATTGGGG
Mouse *Acta2* Forward Primer	GTCCCAGACATCAGGGAGTAA
Mouse *Acta2* Reverse Primer	TCGGATACTTCAGCGTCAGGA

Supplementary references

[1] Furuta K, Guo Q, Pavelko KD, et al. Lipid-induced endothelial vascular cell adhesion molecule 1 promotes nonalcoholic steatohepatitis pathogenesis. J Clin Invest 2021;131.
[2] Guo Q, Furuta K**,** Aly A, et al. Isolation and Characterization of Mouse Primary Liver Sinusoidal Endothelial Cells. J Vis Exp 2021.
[3] Huebert RC, Jagavelu K, Liebl AF, et al. Immortalized liver endothelial cells: a cell culture model for studies of motility and angiogenesis. Lab Invest 2010;90:1770-1781.
[4] Muller WA, Luscinskas FW. Assays of transendothelial migration in vitro. Methods Enzymol 2008;443:155-176.
[5] Sullivan DP, Dalal PJ, Jaulin F, et al. Endothelial IQGAP1 regulates leukocyte transmigration by directing the LBRC to the site of diapedesis. J Exp Med 2019;216:2582-2601.
[6] Krishnan A, Abdullah TS, Mounajjed T, et al. A longitudinal study of whole body, tissue, and cellular physiology in a mouse model of fibrosing NASH with high fidelity to the human condition. Am J Physiol Gastrointest Liver Physiol 2017;312:G666-g680.
[7] Ibrahim SH, Hirsova P, Tomita K, et al. Mixed lineage kinase 3 mediates release of C-X-C motif ligand 10-bearing chemotactic extracellular vesicles from lipotoxic hepatocytes. Hepatology 2016;63:731-744.
[8] **Guo Q, Furuta K**, Lucien F, et al. Integrin beta1-enriched extracellular vesicles mediate monocyte adhesion and promote liver inflammation in murine NASH. J Hepatol 2019;71:1193-1205.
[9] Atkinson JM, Rank KB, Zeng Y, et al. Activating the Wnt/beta-Catenin Pathway for the Treatment of Melanoma--Application of LY2090314, a Novel Selective Inhibitor of Glycogen Synthase Kinase-3. PLoS One 2015;10:e0125028.
[10] Zhao P, Sun X, Chaggan C, et al. An AMPK-caspase-6 axis controls liver damage in nonalcoholic steatohepatitis. Science (New York, NY) 2020;367:652-660.
[11] Jeffers A, Qin W, Owens S, et al. Glycogen Synthase Kinase-3beta Inhibition with 9-ING-41 Attenuates the Progression of Pulmonary Fibrosis. Sci Rep 2019;9:18925.
[12] Tomita K, Kohli R, MacLaurin BL, et al. Mixed-lineage kinase 3 pharmacological inhibition attenuates murine nonalcoholic steatohepatitis. JCI Insight 2017;2.
[13] Kleiner DE, Brunt EM, Van Natta M, et al. Design and validation of a histological scoring system for nonalcoholic fatty liver disease. Hepatology 2005;41:1313-1321.
[14] Wegner KA, Keikhosravi A, Eliceiri KW, et al. Fluorescence of Picrosirius Red Multiplexed With Immunohistochemistry for the Quantitative Assessment of Collagen in Tissue Sections. J Histochem Cytochem 2017;65:479-490.
[15] Bredfeldt JS, Liu Y, Pehlke CA, et al. Computational segmentation of collagen fibers from second-harmonic generation images of breast cancer. J Biomed Opt 2014;19:16007.
[16] Bradski G. The OpenCV library. Dr Dobbs J 2000;25:120-+.
[17] Li J, Van Vranken JG, Pontano Vaites L, et al. TMTpro reagents: a set of isobaric labeling mass tags enables simultaneous proteome-wide measurements across 16 samples. Nat Methods 2020;17:399-404.
[18] Perez-Riverol Y, Bai J, Bandla C, et al. The PRIDE database resources in 2022: a hub for mass spectrometry-based proteomics evidences. Nucleic Acids Res 2022;50:D543-D552.
[19] Chen H, Lau MC, Wong MT, et al. Cytofkit: A Bioconductor Package for an Integrated Mass Cytometry Data Analysis Pipeline. PLoS Comput Biol 2016;12:e1005112.